X-Ray Polarimetry Studies of LMXBs

Master Thesis

Handed in by:	Anand Waghmare
Matriculation number:	6033581
First supervisor:	Prof. Andrea Santangelo
Second supervisor:	Dr. Lorenzo Ducci
Advisor:	Dr. Ruben Farinelli
Sumbitted on:	April 23, 2024

Eberhard Karls Universität Tübingen
Institut für Astronomie und Astrophysik (IAAT)

Declaration of authorship

I confirm that I have written this thesis unaided and without using sources other than those listed and that this thesis has never been submitted to another examination authority and accepted as part of an examination achievement, neither in this form nor in a similar form. All content that was taken from a third party either verbatim or in substance has been acknowledged as such.

City, Date

Name, Signature

Abstract

This thesis presents a polarimetric analysis for four neutron star low-mass X-ray binaries (NS-LMXBs) - Cygnus X-2, XTE J1701-462, GX 9+9, and GX 5-1, utilizing data from the Imaging X-ray Polarimetry Explorer (IXPE). It is followed by simulation to determine the individual contribution to polarization from the boundary layer (BL) of the NS-LMXBs. The analysis revealed significantly higher polarization degree (PD) values in the case of XTE J1701-462 and GX 5-1 in comparison to Cygnus X-2 and GX 9+9. The polarimetric values obtained also suggest a dominant contribution from the BL, which possibly is a cumulative contribution of disk reflection effects. The simulation imposes upper limits on the BL polarization, and thus indirectly constrains external mechanisms of polarization as well. Even with a limited spectral range, the analysis via IXPE data is able to give valuable insights into the polarimetric characteristics of LMXBs.

Contents

1 Introduction

In December 1933, Fritz Zwicky and Walter Baade proposed that dense compact objects could be formed as a result of a supernova in a main star, which they termed neutron stars. However, it was only in 1967 that Jocelyn Bell and Antony Hewish observed periodic signals in the radio band, which was later confirmed to be a pulsar and hence a confirmation of the existence of neutron stars. These objects since then have remained in high interest of scientists in unravelling their various characteristics.

When a massive star (> 10 $M_{\odot}$) evolves into a red giant and then subsequently collapses under its own gravity, a compact object may be formed as a result. Depending upon the initial mass of such a star, the endpoint could be a black hole or a neutron star. Such compact objects are often found in binary systems, along with a companion optical star or another compact object. One such class of system is a low-mass X-ray binary (LMXB), where there is a compact object and a companion low-mass star (< 1 $M_{\odot}$). Such systems are powered by accretion.

LMXBs have long been a mystery in terms of the accretion geometry, and emission mechanisms involved. Which of the regions of geometry are sources for the Comptonized emission and how do these systems evolve with changing accretion rates, are some questions researchers aim to address (Farinelli et al. 2023). In the last few decades, advancements were made in spectroscopy but now with recent developments in X-ray polarimetry, and the launch of Imaging X-ray Polarimetry Explorer (IXPE), a new window has opened to look into these complex questions for further investigation. Through this thesis, the IXPE data has been utilized to probe into the polarimetric properties of four LMXBs - Cygnus X-2, XTE J1701-462, GX 9+9 and GX 5-1 (all hosting a neutron star) - and determine the regions responsible for the emissions observed. Initially considering the contributions from the accretions disk and a boundary layer (BL) around the neutron star, external contributions to the observed signals were also considered. To further strengthen the analysis, a simulation was carried out to establish an upper limit on the contribution of the BL to the total polarization.

This work aims to investigate the polarimetric properties of LMXBs and infer from them the information regarding the geometric structure around the neutron star and the sources of polarized emission from these systems, with the help of IXPE data and numerical simulations. The chapter 2 begins with an introduction to LMXB and how they can be further classified based on their accretion properties, spectral observations and more. The concept of polarization has been explained and the context of polarization in LMXBs was introduced. In chapter 3, the IXPE mission has been described along with instruments involved in the observatory. The methodology for the polarimetric analysis for the four sources has been presented in detail in chapter 4. Results of the analysis have been discussed in the same chapter, presented in a comparison with the published works on the corresponding sources. Chapter 5, describes the simulation work to estimate the BL polarization in a LMXB system. The implications of all the results have been discussed and a conclusion has been proposed in the chapter 6.

2 Astrophysical Background

Within the wider perspective of astrophysics, this thesis is about LMXBs, harbouring neutron stars, with an emphasis on the particular characteristic of polarization. A comprehensive discussion on these topics will be presented in the following sections of this chapter.

Beginning with defining LMXBs, the accretion mechanisms in LMXBs will looked at in more detail, some of their broad categories shall also be discussed briefly. In later parts, the property of polarization discussed and its origin in the context of LMXBs will be setup as well. This chapter is largely inspired by the the book by Longair and the Handbook of X-ray Astronomy by Bambi and Santangelo (Bambi and Santangelo 2022).

2.1 Low Mass X-ray Binaries

By definition, LMXBs are binary systems which consist of a compact object, either a neutron star or a black hole, that accretes gas from a companion star less massive than the compact primary, and typically the companion star is less than 1 $M_{\odot}$. Most of the LMXBs can be found in the Galactic bulge and in globular clusters, which also points towards the fact that they belong to an old stellar population. Many of these systems are powered by an accretion disk around the compact object, which is fed by a Roche-Lobe overflow (RLO) of the companion star. LMXBs differ from HMXBs firstly in terms of the mass of the companion star. HMXBs host a companion which is more massive, typically above 6 $M_{\odot}$, which also suggests that HMXBs belong to a younger population found typically in the Galactic plane. Table 1, shows some primary differences between two. Both LXMBs and HMXBs belong a broader class defined as X-ray Binaries, which are classified according to the compact object they host. Fig 1, depicts the different categories of XRBs.

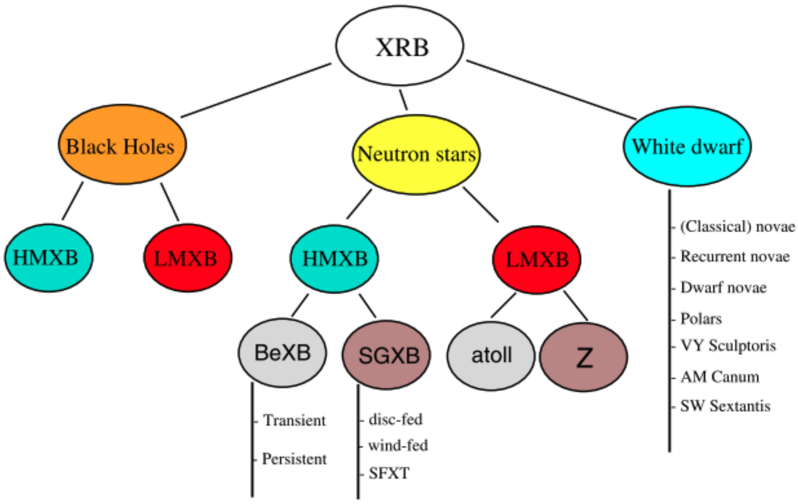

Figure 1: Classification of X-ray binaries (adapted from Reig 2011).

Table 1: The 2 major categories of X-ray sources with strong emission (Tauris and Van Den Heuvel 2010)

	HMXB	**LMXB**
X-ray spectra	Hard band ($\geq$ 15keV)	Soft band ($\leq$ 10keV)
Time variability	periodic X-ray pulsations	X-ray bursts
Accretion process	Wind	Roche-lobe overflow
Accretion timescale	10^5 yr	10^7 - 10^9 yr
Compact object magnetic field	$> 10^{12}$ G	$< 10^{11}G$
Spatial distribution	Galactic plane	Galactic center and spread around the plane
Stellar age	Young, $< 10^7$ yr	Old, $> 10^9$ yr
Companion star	Luminous, early-type O(B) stars	Faint, blue optical counterparts

The dominant emission process in the LMXBs is accretion from the companion star onto the compact object. In many LMXBs the accretion process occurs through RLO. The equation 2.1 describes equipotential surfaces of a rotating binary system, considering a rotating frame of reference, with a constant potential.

$$\phi = \frac{GM_1}{r_1} + \frac{GM_2}{r_2} - \Omega^2 r^2 = \text{constant} \tag{2.1}$$

Here, r is the radial distance from the centre of momentum of the binary system and r_1 and r_2 are the distances of the objects with masses M_1 and M_2 respectively, to the point at r. Figure 2 shows the equipotential surfaces of a binary system.

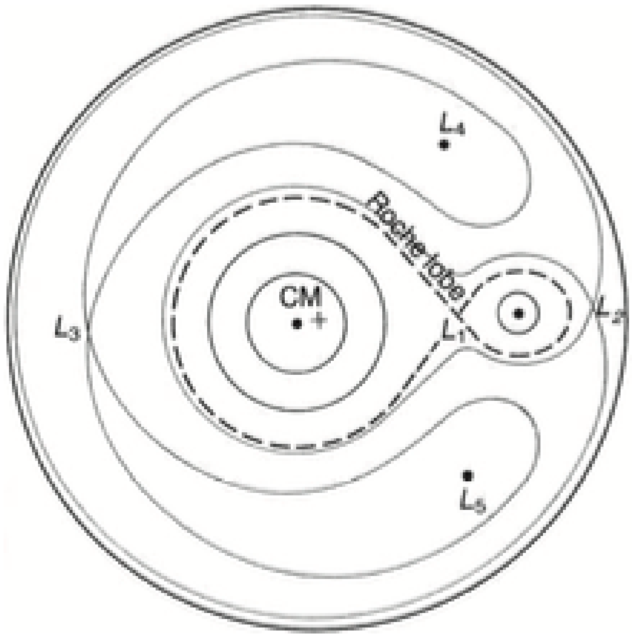

Figure 2: The figure depicts a schematic representation of equipotential surfaces of a binary system with unequal masses. The equipotential surface connecting both the objects is referred to as the Roche lobe of the system, and the two lobes connect at the inner Lagrangian point L_1. The other equilibrium points labelled from L_2 to L_5 are also termed as Lagrangian points. Adapted from: Shapiro and Teukolsky 1983.

In such close binaries, the companion star evolves off the main sequence, The consequence of this leads to its expansion, may be into a red giant, to fill its Roche lobe. Post this, the matter looks for the lowest gravitational potential and eventually crosses the Lagrangian point L_1, to later get locked gravitationally onto the compact object. If the angular momentum of the falling matter is significant, an accretion disk is then formed around the compact object, draining the matter from its companion. This mass transfer leads up to temperatures of millions of Kelvin, and thus releases most of its emissions in the X-ray range. Apart from the accretion mechanism, sometimes LMXBs can be powered by stellar winds and other processes too. Typical luminosities for LMXBs could be between 10^{33}-10^{38} erg/s (Bahramian and Degenaar 2023).

based on binary configuration inferred from observations, and their accretion properties, LMXBs can be divided into sub-classes. The following classification is based on the work of (Bahramian and Degenaar 2023).

Canonical Roche-lobe overflow with main sequence or giant stars

The majority of LMXBs consist of a main sequence, sub-giant or red giant stars that eventually fill the Roche-lobe and initiate the mass transfer onto the compact object in the form of an accretion disc. In such cases, the orbital period is typically in the order of hours. We can see the depiction of this case in Fig (3). Most LMXBs in this category display a transient behaviour which is characterised by outbursts reaching approximately 0.01-0.5 L_{Edd} compared to their luminosity of $\leq 10^{-5}$ L_{Edd} during their quiescence stage (Bahramian and Degenaar 2023).

Ultra-compact X-ray binaries (UCXBs)

When the orbital period of the binaries is very short, about $\leq$ 80 minutes, then these binaries get classified as Ultra-compact binaries (Bahramian and Degenaar 2023). In such cases, to fill the Roche lobe, only sub-dwarf or white dwarf stars are viable candidates that are small enough to fit into the orbit. These stars are primarily burning helium. Measuring the orbital period through direct observation of orbital modulation has been the key method in identifying UCXBs. Fig (3) depicts this category.

Eclipsing LMXBs

The category of eclipsing LMXBs is more like an observational perspective rather than being a separate class. When the binary is viewed at very high inclination angle $\sim 90^\circ$ of the orbital plane from our viewing reference, different properties like eclipse mapping (Baptista 2001), evolution of orbital period on different timescales (Chou 2014), jet physics (Maccarone et al. 2020), can be understood better by studying these eclipses.

Wind-fed accretion in LMXBs

These LMXBs are also known as symbiotic X-ray binaries (SyXBs) and are unique for not exhibiting a Roche-lobe overflow. The spectrum in this case is usually in the optical and NIR range and is dominated by the companion star. There are at times some spurts of wind accretion during enhanced X-ray activity and we can see strong hydrogen emission lines (Chakrabarty and Roche 1997).

Magnetically-channeled accretion in LMXBs: X-ray pulsars

In this sub-class of LMXBs, matter from the inner part of the accretion disk is carried out along the magnetic field lines onto the compact object (NS in this case) and onto the magnetic poles (Bahramian and Degenaar 2023). This leads to the formation of hotspots on the NS and we witness X-ray pulsations attributed to the spin period of the NS. About 20% of these NS-LMXBs showing pulsations in the range of approximately 1-10 ms are called Accreting Millisecond X-ray Pulsars (AXMPs) (Campana and Di Salvo 2018).

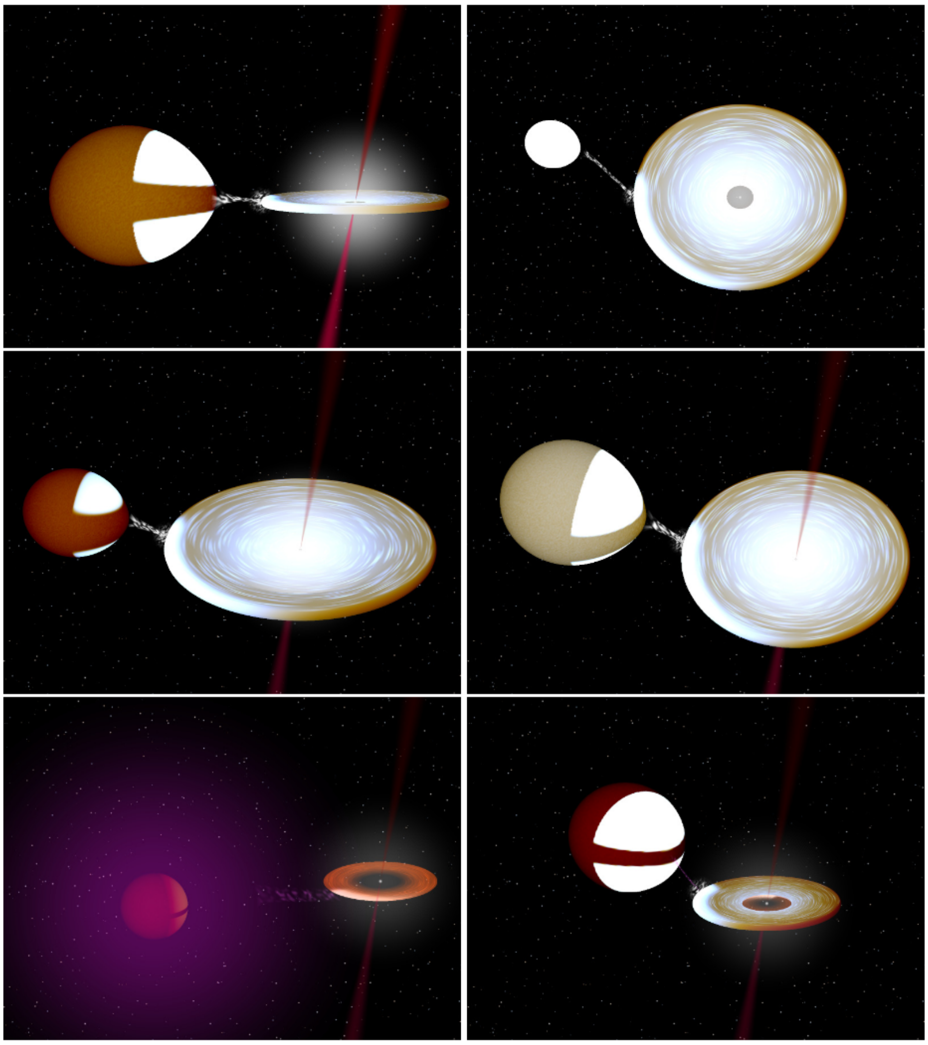

Figure 3: This image depicts various configurations of LMXBs. Top-left: a transient eclipsing LMXB during outburst (Ex: GRS 1747-312). Top-right: a persistent ultra-compact X-ray binary with a low inclination angle (Ex: 2S 0918-549). Middle-left: V404 Cyg during an outburst (transient BH-LMXB). Middle-right: Scorpius X-1 (persistent NS-LMXB). Bottom-left: GC 1+4 (SyXB). Bottom-right: IGR J17062-6143 (very faint X-ray binary). These visualisations were produced using the publicly available BINSIM code. Adapted from: Bahramian and Degenaar 2023.

It is also important to mention the categorisation of LMXBs based upon the correlations between their spectral colors and Fourier timing properties at X-ray wavelengths (Hasinger and van der Klis 1989), into two classes: Z and atoll sources. Typically in astrophysics, Hardness ratios (HR) are usually defined as the ratio of counts in different wavebands (HR = b/a) or the ratio of the difference and sum of counts in two wavebands (HR = (b-a)/(b+a)) , a and b are counts in two wavebands A and B Jin et al. 2006. From these ratios, hardness intensity diagrams (HID) and color-color diagrams (CCD) can be derived. When we plot the intensity in different energy bands in a CCD, some of the LMXBs trace out an unmistakable "Z"-shaped pattern. These are categorised as Z sources. It is believed that such sources might be accreting around the Eddington limit. On the other hand, if the system traces out more like a "C"-shaped pattern in the CCD, it gets classified as an atoll source. These are believed to be well below the Eddington limit (Bahramian and Degenaar 2023). Usually, in the case of the traditional Z sources, a full track is traced out on time scales as short as a day, while atoll sources form their CCDs on much longer time scales of 30-100 days (Bahramian and Degenaar 2023). Some examples of the CCDs of these sources are shown in the Figure 4.

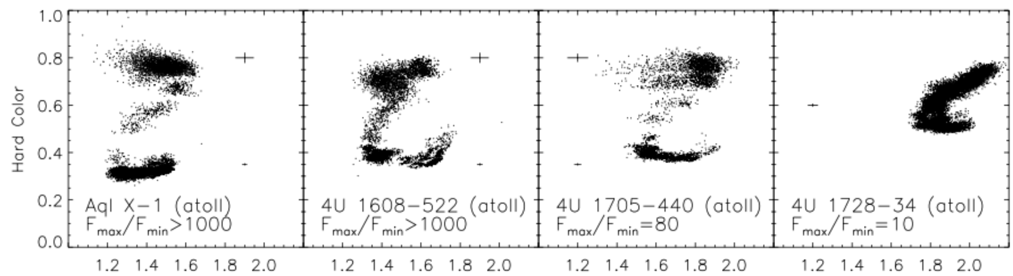

(a) CCDs for atoll sources.

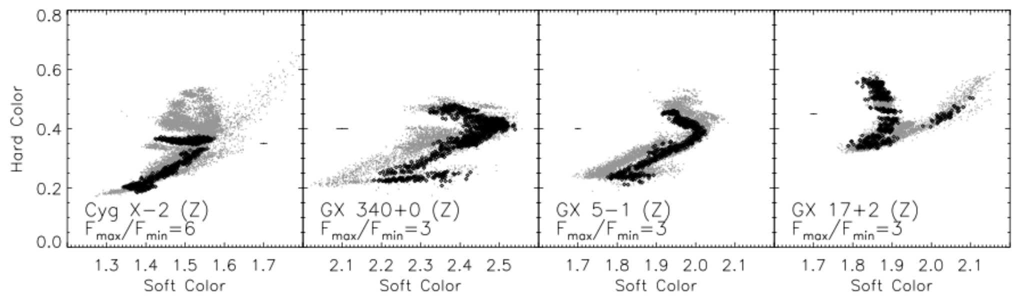

(b) CCDs for Z sources.

Figure 4: Color-color diagrams from five years of pointed RXTE PCA observations Bahramian and Degenaar 2023.

2.2 Polarization

This thesis revolves around a characteristic of an electromagnetic wave, called polarization. The polarization state of an electromagnetic wave corresponds to the alignment of oscillation of its electric field. Now, the wave can be polarized in different states: linearly polarized light, where the orientation of the vibration is constant, and circularly or elliptically polarized light, where it varies periodically with time. When the wave carves out a circular pattern in space while propagating, it is termed circularly polarized light. Elliptically polarized light can be visualized as a combination of linearly and circularly polarized light. Finally, there is unpolarized light, where the polarization state of the beam changes continually and randomly with time.

This section is inspired from the book (Mignani et al. 2019).

2.2.1 Stokes Parameters

A useful way of describing the state of polarization (SOP) of an electromagnetic wave, is to use the mathematical toolkit called the Stokes parameters. While measuring the SOP we tend to use the calculations derived from the Stokes parameters. These parameters are equivalent to the time-averaged measurement of the orientation of the electric field (Shucliff 1984, Born and Wold 1999, Goldstein 2011). They can be expressed in the following fashion:

$$\mathbf{s} = \begin{pmatrix} s_0 \\ s_1 \\ s_2 \\ s_3 \end{pmatrix} = \begin{pmatrix} I_{total} \\ I_H - I_V \\ I_{+45^\circ} - I_{-45^\circ} \\ s_3 \end{pmatrix} = \begin{pmatrix} I \\ Q \\ U \\ V \end{pmatrix} \tag{2.2}$$

In the above equation, I_{total} represents the total intensity of the light, I_H and I_V are the intensities of the light resolved into its horizontal and vertical components, respectively. I_{+45° and I_{-45° correspond to the radiation linearly polarized at +45° and -45° respectively. I_R and I_L represent the right-circularly and left-circularly polarized light respectively.

The polarization degree (PD) of an electromagnetic wave refers to the ratio of polarized light to the total intensity. This fraction is denoted in the following way:

$$PD = \frac{\sqrt{(s_1)^2 + (s_2)^2 + (s_3)^2}}{s_0} = \frac{\sqrt{(Q)^2 + (U)^2 + (V)^2}}{I} \tag{2.3}$$

If the light is only linearly polarized, then we can calculate the degree of linear polarization like:

$$PD_L = \frac{\sqrt{(s_1)^2 + (s_2)^2}}{s_0} = \frac{\sqrt{(Q)^2 + (U)^2}}{I} \tag{2.4}$$

The angle of polarization (PA), the preferred angle of radiation's electric field, can be written as:

$$\theta = \frac{1}{2} tan^{-1} \left(\frac{U}{Q} \right) \tag{2.5}$$

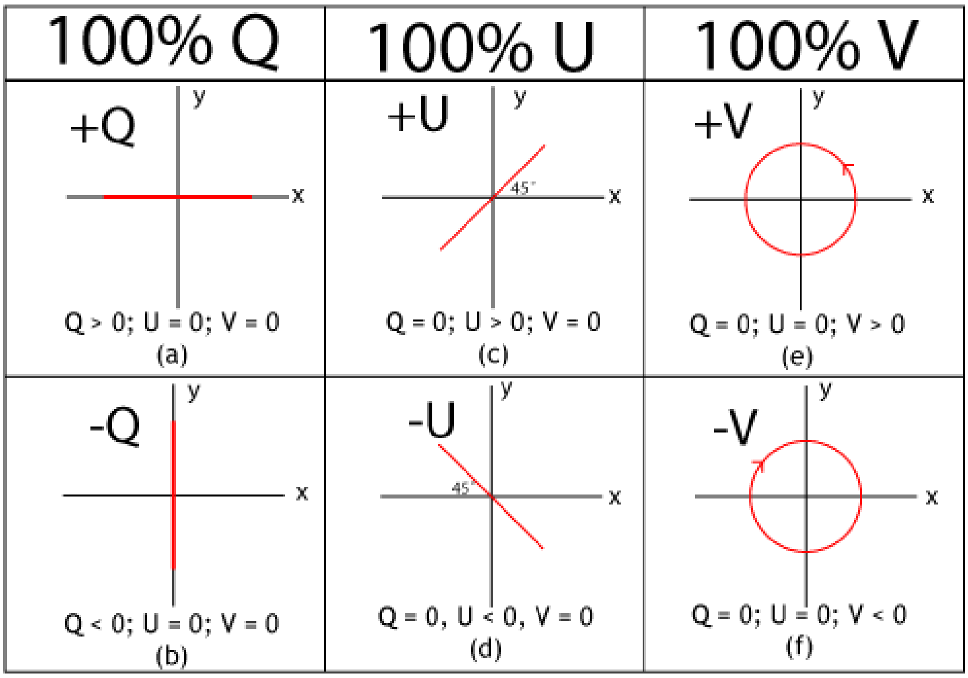

Figure 5: The image depicts different states of polarization with their corresponding Stokes parameters. (image credit: Dan Moultan)

In the context of astrophysics, polarization can be produced in many ways such as, directly from radiation processes like synchrotron and cyclotron emission, scattering of radiation, and differential absorption of radiation passing through interstellar medium. Since this characteristic is directly related to the physical activities and geometrical structures of and around a body, polarization provides a unique probe to measure certain parameters which otherwise would not have been possible.

In the context of LMXBs, we tend to analyse the X-ray emission as a result of the accretion mechanisms. Now these emissions can be polarized. The reasons can be again dependent upon the origin of the polarization, be it intrinsic to the compact object or the accretion disk, or maybe from the reflection off a disk surface, some other processes or just a combination of all of these. Utilizing the measurements of polarization from these objects helps in a better understanding of the geometrical structure of these systems, the accretion processes involved and much more.

3 The Imaging X-ray Polarimetry Explorer (IXPE) Mission

The Imaging X-ray Polarimetry Explorer (IXPE) mission was launched on December 09, 2021, on a Falcon-9 rocket from the Kennedy Space Center. It is a Small Explorer Mission designed specifically to investigate a new window of studying the phenomenon of X-ray Polarimetry. The primary objectives of this mission were to investigate the radiation processes and detailed characteristics of specific cosmic X-ray sources; and to survey quantum and general relativistic effects in extreme environments. X-rays in the energy range of 2–8 keV are the focus of IXPE investigations. The information provided in this chapter is inspired by the user guides for the observatory and instruments provided by the IXPE team.

IXPE mission was initially dedicated to a 2-year period in which the plan was to observe cosmic objects like black holes, pulsars, active galactic nuclei, accreting X-ray binaries, supernova remnants and a few more. Properties like ordered magnetic fields, aspheric matter distributions, general relativistic coupling to black hole spin and other anisotropies, in some of these objects are uniquely probed by polarization and are not measurable otherwise.

The mission is an international collaboration led by NASA Marshall Space Flight Center (MSFC) and the Italian Space Agency (ASI), along with a few other institutions (shown in Fig 1). ASI contributed to the polarization-sensitive detectors, invented and developed at the Istituto Nazionale di AstroFisica (INAF) and the Istituto Nazionale di Fisica Nucleare (INFN). Orbiting Solar Observatory-8 (OSO-8), launched in 1975, had a polarimeter on board, which carried out the first measurements of such kind. The investigating team led by Prof Robert Novick of Columbia University, were successful in making polarimetric measurements of the Crab Nebula, thus setting the foundation of X-ray polarimetry. IXPE's objective is to enhance the sensitivity of polarization detectors by at least 2 orders of magnitude.

Figure 1: The IXPE team and responsibilities (image credit: User Guide - Observatory IXPE)

The observatory hosts 3 identical telescopes, each consisting of a mirror module assembly (MMA) with polarization-sensitive detectors (so-called Gas Pixel Detectors or GPDs) at the focus. A 4 m focal length is provided by an extending boom. An overview of the structure can be seen in Fig 2.

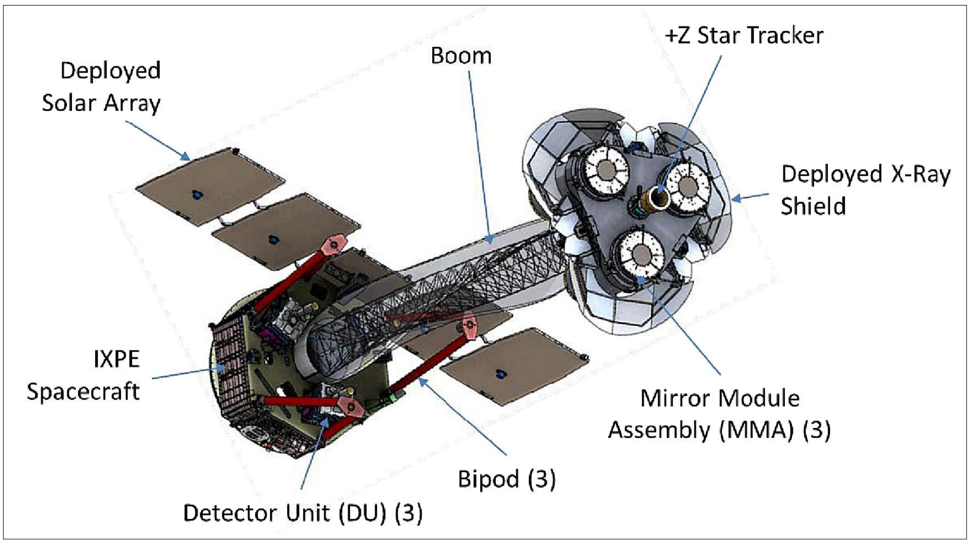

Figure 2: The deployed configuration of the IXPE observatory. (image credit: IXPE team)

IXPE detects polarization by noting the distribution of the location of starting points of tracks left behind by individual photo-electrons on GPDs (this helps in imaging) and their direction (helps in the investigation of polarimetric values).

Parameter	**Value**
Energy range	2-8 keV
Field of View	> 11’
Angular resolution	28"
Number of mirror modules	3
Number of shells per module	24

Table 2: Key parameters of IXPE observatory.

3.0.1 Detector units (DUs)

The DUs are the core of the IXPE payload. There are 3 identical DUs, each corresponding to its MMA. Each DU comprises its own electronics, which communicate with the onboard computer individually. Situated at the focus of each MMA, these units provide position sensitivity, energy determination, timing information and polarization sensitivity. The DU consists of a Gas Pixel Detector (GPD), which is filled with a special gas (DME - Dimethyl Ether). Figure 3 shows a schematic representation of a GPD.

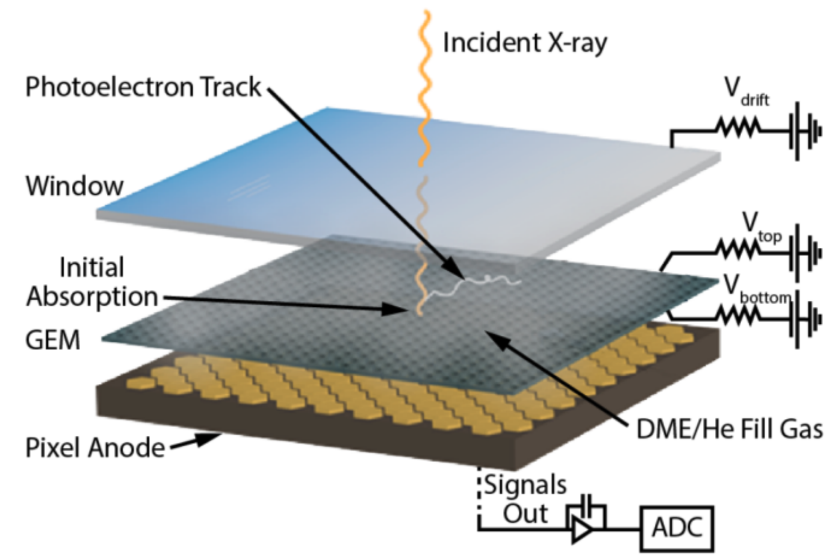

Figure 3: Schematic of the Gas Pixel Detector (GPD). (image credit: IXPE team)

Once an X-ray enters through the beryllium window, it interacts with the DME fill gas. This interaction results in the release of a photoelectron, which leaves behind a trail of ionization. The track drifts through a Gas Electron Multiplier (GEM) and is read out on a pixelated anode. The information about the initial interaction point and detector coordinates of all electron clusters read along the track, is stored in Level 1 files. This is the raw data that is initially generated. To make use of this raw data for scientific analysis, several steps have to be performed. Some of the steps include a screening of tracks likely related to particle background, integration of total charge collected for a given track, energy calibration, reconstruction of track direction and corresponding Stokes parameters for individual events, and more. The IXPE consortium executes all the necessary steps and the processed data is available in the form of Level 2 files.

IXPE's sensitivity is a result of long observations of known X-ray sources, over multiple orbits until the desired sensitivity is achieved and the observation is complete. The attitude determination and control subsystem of the craft allows IXPE to remain pointed at the desired target for up to many days at a time.

4 Data Analysis and Results

In this chapter, the analysis of IXPE data for the four different LMXBs - Cygnus X-2, XTE J1701-462, GX 9+9 and GX 5-1, is presented. The analysis is broadly divided into two parts: a model-independent analysis (PCUBE) and a model-dependent analysis (spectro-polarimetry). Each aspect will be explored in detail in the upcoming sections. As we move through the subsections, the work will include data collection, an introduction to the tools required for scientific analysis, data processing, and, finally, the presentation of the analysis results.

One of the primary objectives of this research work was to replicate the polarimetric analysis, with the available resources, conducted on IXPE observations as previously disseminated by members of the IXPE consortium. Hence, certain aspects of the methodological framework, data handling and grouping, were guided by these published works.

4.1 Data collection and Analysis tools

The data for all IXPE observations has been made available by the NASA High Energy Astrophysics Science Archive Research Center (HEASARC) on its website[1]. When searching for a source's IXPE observation data, there are two different data files that can be downloaded: Level 1 and Level 2. As mentioned previously, Level 1 data consists of raw information that includes details of the initial interaction points, direction, and charge of the photo-electron tracks corresponding to an event, etc. However, the IXPE consortium has provided pre-processed data in the form of Level 2 files, which are ready for further scientific analysis. For all four sources (Cygnus X-2, XTE J1701-462, GX 9+9, and GX 5-1), I have used Level 2 data as the starting point.

[1] Link to the HEASARC archive : `https://heasarc.gsfc.nasa.gov/docs/archive.html`.

IXPE data can be analyzed using the HEAsoft toolkit, readily available on the HEASARC website. However, these tools are not mission-specific and therefore have limited applicability in the context of IXPE. Nevertheless, a new framework called *ixpeobssim* is available, which can be utilized through command-line tools or a Python interface directly.

The *ixpeobssim* framework is a simulation and analysis framework specifically developed for the IXPE mission. It is designed not only to produce realistic simulated observations, based on a source model and appropriate response functions of the telescope, but also comes with a suite of post-processing applications supporting spatial, spectral, and temporal models necessary to analyze polarized X-ray sources. Built on the Python programming language, it leverages prominent scientific libraries such as *numpy*, *matplotlib*, and *Astropy* (Baldini et al. 2022).

In this analysis, I have made use of *ixpeobssim* (version 30.2.3) in conjunction with the HEAsoft (version 6.31.1) tool `XSPEC`. While the former was employed to establish analysis parameters, extract images and light curves, intensity (I), and Stokes (Q and U) spectra, as well as for data grouping, the latter was mostly utilized in the model-dependent (spectro-polarimetric) analysis of the grouped data. Some noteworthy commands in *ixpeobssim* include:

- `xpobssim`: Generate a list of photons for a specific time of observation using a source model and a set of instrument response functions.
- `xpselect`: select specific subsets of photons from a provided event file by considering factors such as energy, direction, time, or phase; produces a new in the process.
- `xpbin`: enables data binning using various that results in output files containing lists of binned events.
- `xpxspec`: perform a spectro-polarimetric fit in `XSPEC`.

The full set of commands and information of the tools can be found in the *ixpeobssim* documentation which is available at: https://ixpeobssim.readthedocs.io/en/latest/.

4.1.1 Data selection and processing

After downloading the Level 2 data, one can notice 3 different FITS files corresponding to each of the three telescopes for an observation. Before starting the analysis, certain parameters were set which are common to all four sources. The instrument response function (IRF) of 'ixpe:obssim:v12' was set, the bin size for the light curves was set to 60, the radius of the source selected to be 1', while the background inner and outer radii were set at 3' and 4', respectively. It is also necessary to mention the energy range within which the analysis will be conducted, at the beginning.

IXPE observed Cygnus X-2 on two separate occasions: the first observation was on 30th of April 2022, while the second was on 5th of May 2022. For the source XTE J1701-462 as well, two observations were carried out: first one on 29th Sept 2022 and the second on 8th Oct 2022. GX 9+9 was observed only once: 9th of Oct 2022. The latest of the four is GX 5-1, which was observed twice: first on 21st March 2023 and second on 13th April 2023. In this study, before initiating the analysis, the data pertaining to Cygnus X-2 from both observations were merged in accordance with the methodology outlined in the work by Farinelli et al. 2023. In the case of GX 5-1, the data set available on the HEASARC archive has only one combined file for both the observations. So, it was split into two separate observations to compare the analysis with Fabiani et al. 2023 (pre-print).

Using the `xpbin` (implementing the `CMAP` algorithm) and *Aplpy* tools, images of the sources were extracted and displayed. It is important to note that the coordinates of the centre of the sources mentioned on the HEASARC archives for the IXPE mission are miss-calibrated. These had to be corrected before extracting any other information from the FITS files. I used the maximum pixel value detection to find the new set of coordinates for the sources. The corrected coordinates have been shown in the table 3. The extracted images for all the sources have been presented in the Fig 1.

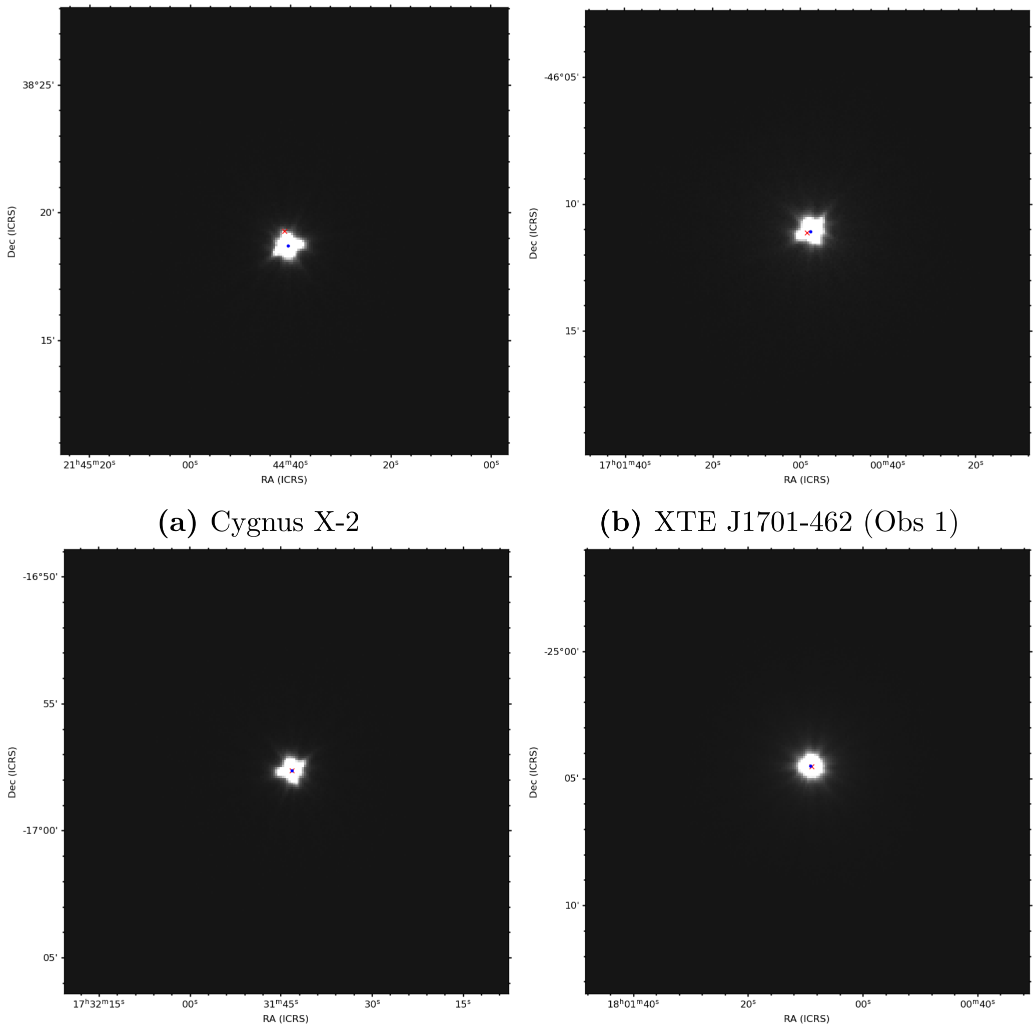

(a) Cygnus X-2 **(b)** XTE J1701-462 (Obs 1)

(c) GX 9+9 **(d)** GX 5-1 (Obs 2)

Figure 1: Extracted images for the 4 analysed LMXBs. The red cross marking shows the original coordinates for the respective source, while the blue dot points the corrected coordinates.

Source	**Old Coordinates** (deg)	**New Coordinates** (deg)
Cygnus X-2	326.171, 38.321	326.169, 38.312
XTE J1701-462	255.244, -46.186	255.24, -46.185
GX 9+9	262.934, -16.961	262.93, -16.96
GX 5-1	270.287, -25.074	270.288, -25.075

Table 3: Corrected coordinates for the four mentioned sources for IXPE observations. The correction is required to accommodate the inaccuracy of IXPE reference system.

Using the '`xpselect`' tool, events for the source and background regions were extracted and compiled into corresponding lists. These lists now can be used for further analysis for extracting light curves ad polarization studies.

Light curves were extracted and binned using the '`xpbin`' tool implementing the '`LC`' algorithm. The extracted light curves have been presented in the Fig 2.

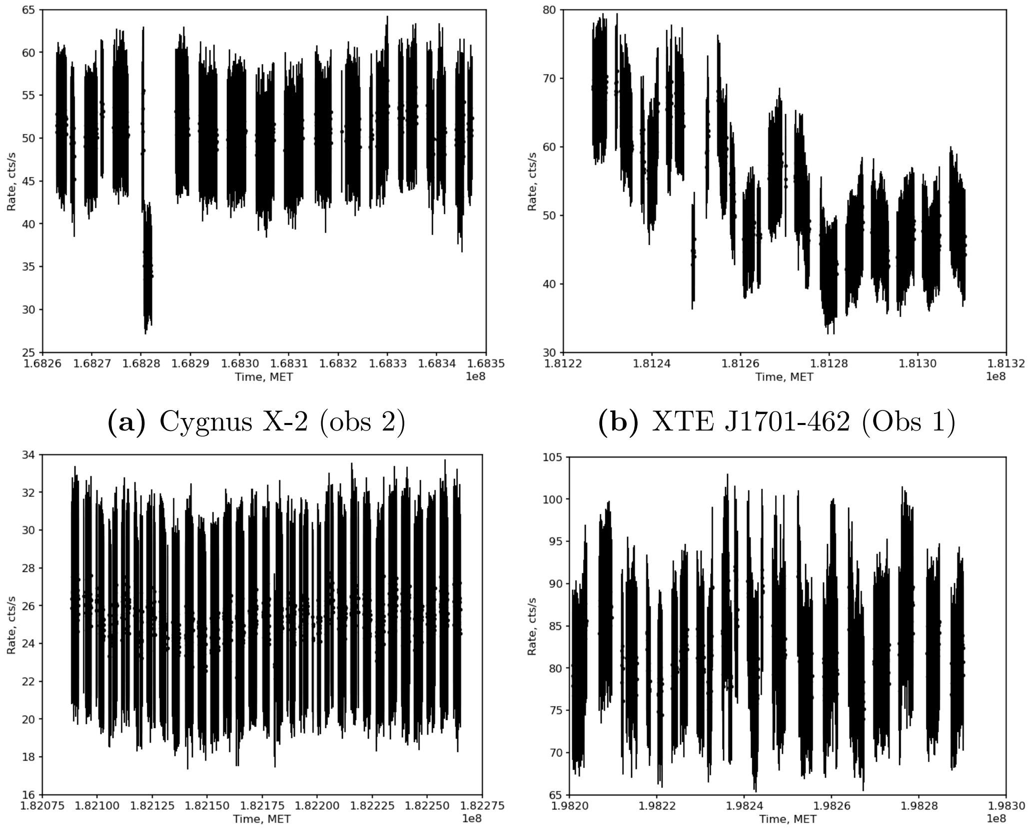

(a) Cygnus X-2 (obs 2) **(b)** XTE J1701-462 (Obs 1)

(c) GX 9+9 **(d)** GX 5-1 (Obs 2)

Figure 2: Extracted light curves for the 4 analysed LMXBs.

After extracting the images and the light curves, the next step is to start the main goal of the analysis: investigating the polarization properties of the emissions. Two different methodologies were followed. A model-independent method which we will refer to as the PCUBE analysis, and a model-dependent analysis - spectro-polarimetric analysis.

4.1.2 PCUBE analysis

This was performed using only the python package of *ixpeobssim*. This again is possible with the '`xpbin`' tool, via the '`PCUBE`' algorithm. This routine computes the I-normalized Stokes parameters Q and U from the event-by-event Stokes parameters of the sample of selected events. The algorithm supports the calculation of the background-subtracted Stokes parameters if a background template is provided

(Negro et al. 2023). This approach has been presented in detail in Kislat et al. 2015.

In this work, I carried out the PCUBE analysis for the 4 souces, in different energy ranges: 2-8 keV, 2-4 keV and 4-8 keV. The results will be discussed in the upcoming sections. The background was subtracted from the source event files. It is worthwhile to mention that this algorithm assumes that PD and PA are independent, but in reality that is not the case. Hence, PCUBE analysis is in this context is a preliminary analysis to a more detailed model based approach.

4.1.3 Spectropolarimetric analysis

Using the event files generated earlier via '`xpselect`', and then binning the data using '`xpbin`' tool via the '`PHA`' algorithm, the I ('`PHA1`') , Q ('`PHAQ`') and U ('`PHAU`') spectra can be extracted separately for the source and the background region. Once the spectra files were generated, '`XSPEC`' was used for further analysis.

For all the sources a standard two component HSS (hard spectral state) model, composed of a multi-color disk and a harder boundary-spreading layer, was used (Popham and Sunyaev 2001). The multi-color disk, using '`XSPEC`', can be modeled using '`diskbb`' and '`diskpn`'. In this work, the former was selected. In the case of modelling the BL, models for a pure black body '`bbodyrad`' or an unsaturated Comptanization model like '`comptt`' could have been used. This work makes use of '`bbodyrad`'. The choices were majorly influenced by the fact that the other models, if chosen, would have caused a degeneracy in the parameter space. IXPE observation data has a limited number of channels and hence the issue could have arisen due to the relatively narrow data pass-band. This prevents the energy cutoff from being constrained (Cocchi et al. 2023).

Authors for the published works on most of these sources have avoided this issue by merging the data of IXPE with other wider energy range missions like NICER (Neutron Star Interior Composition Explorer), NuSTAR (Nuclear Spectroscopic Telescope Array), AstroSat and INTEGRAL (The INTErnational Gamma-Ray Astrophysics Laboratory). This has allowed them to include components like '`comptt`', '`nthComp`' and in some cases even a reflection component. In this context, the research presented in this thesis serves as a cross-validation of the polarization characteristics obtained in prior publications, while stating limitation of the IXPE data if used alone. It employs a model, distinct from those employed in the published works, yet important within the framework of LMXBs.

The final model used for spectro-polarimetric analysis, in this thesis, has the following components:

- `Const`: it is a normalising cross-calibration multiplicative factor. It accounts for uncertainties in the effective areas of telescope.
- `Polconst`: this component is responsible for the calculation of the PD and PA.
- `tbabs`: it takes into account the low-energy absorption due to the ISM (interstellar medium) and other other factors.
- `diskbb`: it models a spectrum from an accretion disk consisting of multiple blackbody components.
- `bbodyrad`: it models a blackbody spectrum with normalization proportional to the surface area.

In `XSPEC`, the model reads out like:

$$< \texttt{const} > * < \texttt{polconst} > * < \texttt{tbabs} > *(< \texttt{diskbb} > + < \texttt{bbodyrad} >) \tag{4.1}$$

Additonally, the polarization contribution from the individual components can also be investigated using a slightly modifying the additive part of the previous model:

$$(< \texttt{polconst} > * < \texttt{diskbb} > + < \texttt{polconst} > * < \texttt{bbodyrad} >) \tag{4.2}$$

For this work the abundances were set according to Wilms et al. 2000. With this analysis, the values for parameters can be found to investigate the geometrical structures involved in the accretion mechanism in LMXBs. A weighted analysis was performed in the case of XTE J1701-462, while the rest of the sources were analysed with unweighted algorithm. The results have been discussed in the following section.

4.2 Results

In this section, the results of the data analysis are presented. We begin with the results of PCUBE analysis with comparison across all the sources, and then move to individual sources comparison with the corresponding published works. In the following section, we will look at the results of the model-independent analysis individually for each source, along with the model-dependent analysis.

		Cygnus X-2	**XTE J1701-462**	**GX 9+9**	**GX 5-1**
2-8 keV	PD (%)	1.19 ±0.19	3.93±0.32	1.02±0.34	3.94±0.26
	PA (deg)	134±5	148±2	70±10	-6±2
2-4 keV	PD (%)	0.98±0.23	3.54±0.39	0.79±0.4	3.79±0.33
	PA (deg)	133±7	150±3	73±15	-4±3
4-8 keV	PD (%)	2.38±0.34	5.89±0.54	2.67±0.63	4.67±0.42
	PA (deg)	138±4	145±3	64±7	-13±3

Table 4: Values for polarization degree (PD) and polarization angle (PA) obtained for the respective LMXBs, for PCUBE analysis. Presented values are for Obs 1 in case of XTE J1701-462, GX 9+9 and GX 5-1. For Cygnus X-2 Obs 1 & 2 have been combined together for the analysis. Errors are in the 1-σ range.

According to Table 4, XTE J1701-462 and GX 5-1 show a high PD ∼4% in the 2-8 keV range, while PD of Cyg X-2 and GX 9+9 remains low ∼1%. A clear trend emerges as it can be seen that the PD increases as we move from 2-4 keV range to 4-8 keV range across all the sources. The PA in the sources seems to be greater in the 2-4 keV range than in 4-8 keV range, except in the case of Cyg X-2. In LMXBs, the polarization induced by electron scattering in an accretion disc is the highest if the system is viewed edge-on and reduces to zero if the inclination angle is $\sim 0°$ (Chandrasekhar 2003). The inclination angle of Cyg X-2 is most likely around $\sim 60°$ (Orosz and Kuulkers 1999). This indicates that the nature of polarization arising from the source is connected not just to the electron scattering in the disc but other factors too. This mostly is the case in the other LMXB systems as well, although the inclination for the other sources is not known.

4.2.1 Cygnus X-2

The binary system of Cygnus X-2 hosts a neutron star as the compact object, the mass of which is $\sim 1.71\ M_{\odot}$ (Casares et al. 1998). The companion object is the optical component of the binary with a mass of $\sim 0.58\ M_{\odot}$ (Casares et al. 1998). It has been observed to have a long orbital period of P = 9.84 days (Cowley et al. 1979). Cyg X-2 has been usually an object of curiosity because of its high X-ray flux $F_X \sim (1-3) \times 10^{-8}\ erg\ cm^{-2}\ s^{-1}$ (Farinelli et al. 2023). From the CCD and hardness-intensity diagram, Cyg X-2 can be classified as a Z source (Hasinger and van der Klis 1989). An important point to note for this system is that a relativistic jet has also been observed. Spencer et al. 2013 have shown with joint observations with Swift/XRT and the VLBI at 5GHz, the presence of a sub-relativistic jet.

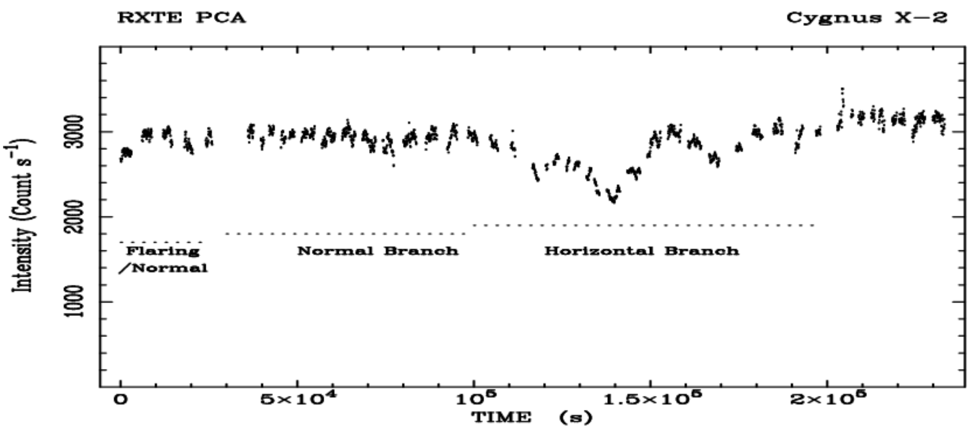

Figure 3: This image depicts background subtracted and deadtime-corrected RXTE PCA light curve of Cygnus X-2 with 64s binning (Bałucińska-Church, M. et al. 2010).

The results for model-independent polarimetic analysis for Cyg X-2 have been shown in the Table 5. I found the PD in the 2-8 keV range for this source to be 1.19±0.19%. This result however differs from that of the published work by Farinelli et al. 2023, which states the PD to be $1.85 \pm 0.87\%$. In a similar manner there are differences between my results and the published one in the 2-4 keV range with values of PD $\sim 1\%$ and $\sim 1.5\%$ respectively, and also in the 4-8 keV range with PD $\sim 2.4\%$

and $\sim 2.8\%$ respectively. The values lie, however, in $2-\sigma$ range. In the case of PA, the values are well within $1-\sigma$ as I found the value of PA in 2-8 keV range to be $135 \pm 5°$ compared to the corresponding published value of PA of $140 \pm 12°$. This discrepancy in the values is attributed to the source data being used for the analysis. The published work from the IXPE consortium by Farinelli et al. 2023, makes use of the Level 1 data, utilizing specialised tools to make that dataset ready for the scientific analysis. Those tools have limited accessibility to people outside the consortium. For my work, I used the Level 2 data which was cleaned and calibrated by the IXPE team. However, at the time of uploading Level 2 files for Cyg X-2, the calibration techniques might not have been fully developed and hence discrepancies could have arisen. Cyg X-2 was one of the first observed sources by IXPE and such deviations are less frequent in the data sets for the sources observed later.

	Cygnus X-2	**Present Work**	**Published Results**
2-8 keV	PD (%)	1.19 ±0.19	1.85±0.29
	PA (deg)	135±5	140±12
2-4 keV	PD (%)	0.98±0.23	1.49±0.26
	PA (deg)	133±7	144±15
4-8 keV	PD (%)	2.38±0.34	2.79±0.56
	PA (deg)	138±4	134±18

Table 5: Values for polarization degree (PD) and polarization angle (PA) obtained for Cygnus X-2 compared to the published work by Farinelli et al. 2023, for PCUBE analysis. Errors are in the 1-σ range.

In Fig 4, we can see the intensity spectra been plotted for Cyg X-2. There are 3 different spectra, each one for the corresponding 3 detectors aboard IXPE observatory. The spectra was fit with the model described in the earlier section except for the polarization component: <`const`> * <`tbabs`> * (<`diskbb`> + <`bbodyrad`>). We can see from the residuals that not only do all the spectra deviate away from the model for most of the energy range, but also deviate from each other. This indicates that the calibration between the three detectors hasn't been optimised in the case of

Cyg X-2 for the Level 2 data. Further spectro-polarimetric analysis was not carried out due to this reason. This limitation was resolved by Farinelli et al. 2023, by using the spectra for Cyg X-2 obtained via NICER to obtain certain parameters, and then integrate with IXPE data later to find the polarimetric values.

Even then, just from the values of PD and PA obtained via PCUBE analysis we can make some significant observations. The radio jet of Cyg X-2 was found to be at $\sim 141°$ (Spencer et al. 2013), which suggests that the PA angle of $131° \pm 4.7°$ is close to parallel alignment with the jet with 2-σ confidence. This suggests that polarization from the accretion disc and a BL co-planar with it, alone, cannot be responsible for the total polarization.

The spectro-polarimetric analysis done by Farinelli et al. 2023 also included two `polconst` components, one for `diskbb` and `comptt` to find their individual contribution to the total polarization. Their model looks like:

$$< \texttt{tbabs} > *(< \texttt{polconst} > * < \texttt{diskbb} > + < \texttt{polconst} > * < \texttt{bbodyrad} >) \tag{4.3}$$

The comptonization component is assumed to arise from the BL around the NS, and the polarization produced will be perpendicular to that produced by the scattering in the accretion disc. They found the contribution to PD from the disc to be 3.3% as upper limit and the PA of $43 \pm 11°$. While the values obtained for comptonization component were with PD of $4.0^{+2.0}_{-1.7}\%$ and PA of $133° \pm 11°$. Hence, polarization from the spreading layer seems to be dominant, and also justifies the PA we observe. It was also suggested that the PD value obtained for comptonization, may also include a reflection component. In this case a BL around the NS might act as a source of photon which then get reflected a few time off the disc causing significant polarization. However, IXPE observation itself is not able to resolve such a component separately.

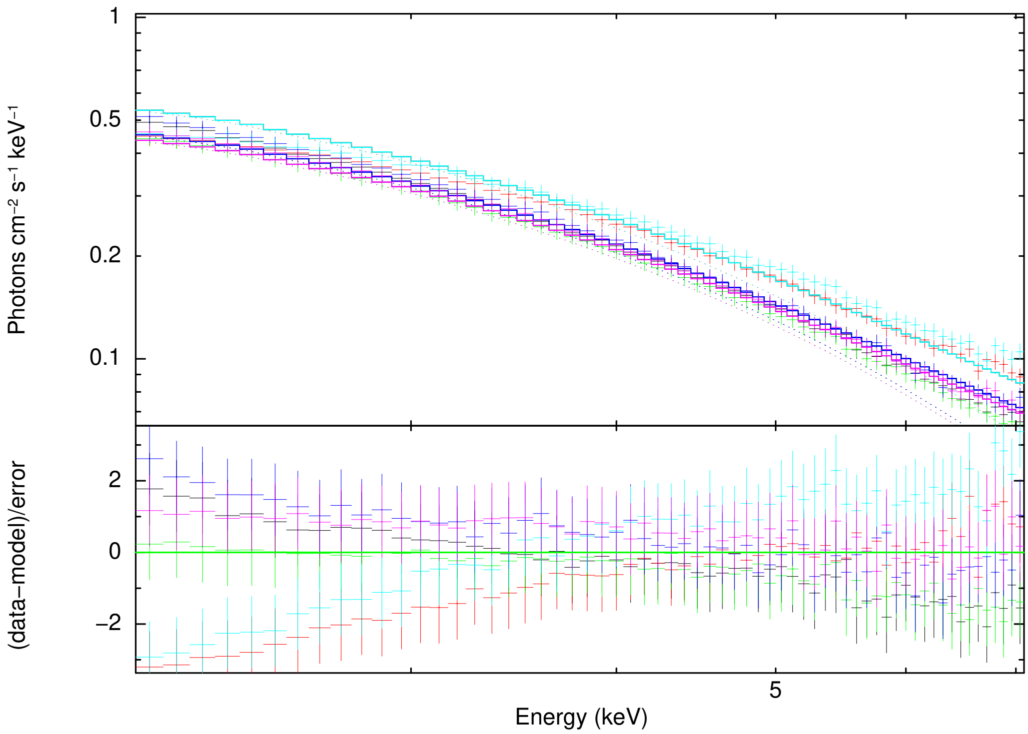

Figure 4: The unfolded intensity spectra for Cygnus X-2 (combined), fitted with the model <const> * <tbabs> * (<diskbb> + <bbodyrad>).

4.2.2 XTE J1701-462

Located at around 8.8 kpc (Lin et al. 2009a) from us, XTE J1701-462 hosts a neutron star. It was discovered in 2006 by (Remillard et al. 2006). The unique feature of this binary system is the fact that it has shown all the spectral states of a NS-LMXB during its 2006 outburst (Lin et al. 2009b). It has been classified as a Z source LMXB. On a CCD, three different branches in a typical Z source are horizontal, normal and flaring branches (HB, NB, FB). Two of these branches, HB and NB, appear in the CCD plot for XTE J1701-462 shown in Fig 5. and it is the only known system to displayed all the three branches till now. Such behaviour has helped scientists determine the physics of different accretion states in an object-unbiased manner (Cocchi et al. 2023). The orbital period for this source has not been determined so far.

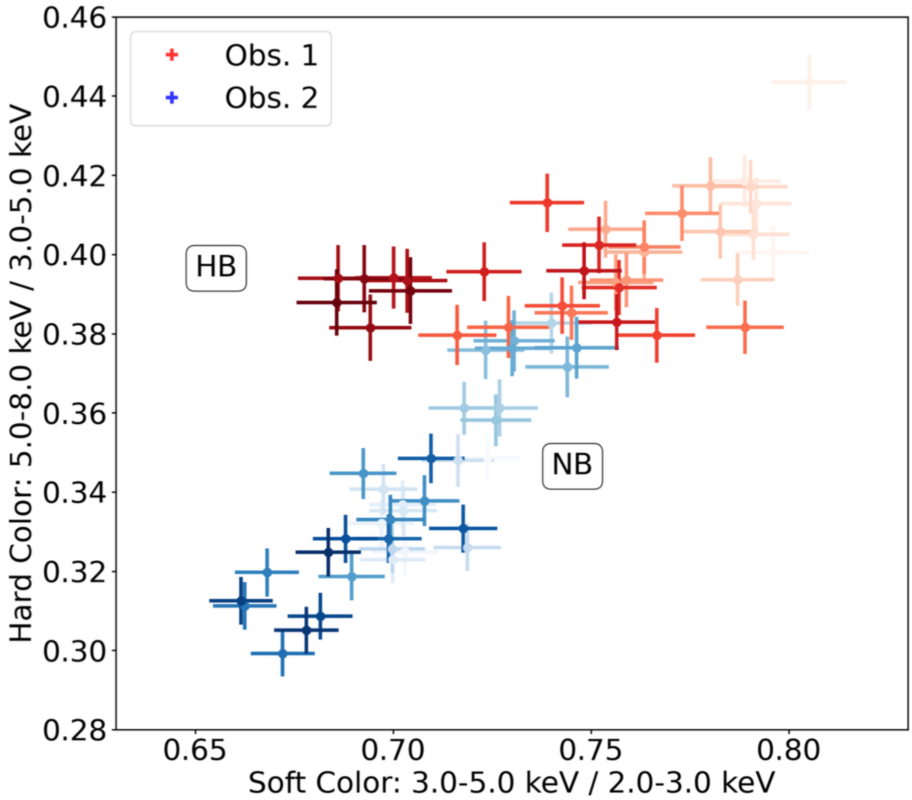

Figure 5: CCD of XTE J1701-462 during two different observations (Sept. 29th and Oct 8th, 2022) is shown. Each point corresponds to 500s integration time (Cocchi et al. 2023).

Upon analysing XTE J1701-462 with PCUBE algorithm, the results shown in Table 6 and Table 7 were obtained, for Obs 1 and Obs 2 respectively. It is evident upon comparison between the two observations that the PD value obtained in Obs 1 is significantly higher than the one for Obs 2. In fact, the value obtained for Obs 2 is below the minimum detectable polarization (MDP) at the 99% confidence level in all the energy bands for the IXPE instrument. When compared to the published values by Jayasurya et al. 2023 for both the observations, the analysed values lie well within 1-σ range.

	XTE J1701-462 (Obs 1)	**Present Work**	**Published Results**
2-8 keV	PD (%)	3.93 ±0.32	3.89±0.36
	PA (deg)	148±2	143±2
2-4 keV	PD (%)	3.54±0.39	4.53±0.36
	PA (deg)	150±3	146±3
4-8 keV	PD (%)	5.89±0.54	5.52±0.6
	PA (deg)	145±3	140±3

Table 6: Values for polarization degree (PD) and polarization angle (PA) obtained for XTE J1701-462 (Obs 1) compared to the published work by Jayasurya et al. 2023, for PCUBE analysis. Errors are in the 1-σ range.

	XTE J1701-462 (Obs 2)	**Present Work**	**Published Results**
2-8 keV	PD (%)	0.57 ±0.29	0.51±0.33
	PA (deg)	-53±15	-
2-4 keV	PD (%)	0.53±0.34	1.60±0.58
	PA (deg)	-46±19	-
4-8 keV	PD (%)	1.12±0.51	0.83±0.33
	PA (deg)	-73±13	-

Table 7: Values for polarization degree (PD) and polarization angle (PA) obtained for XTE J1701-462 (Obs 2) compared to the published work by Jayasurya et al. 2023, for PCUBE analysis. Errors are in the 1-σ range.

Following the PCUBE analysis, a model-dependent spectro-polarimetric analysis was also performed for both the observations. The intensity spectra for Obs 1 is shown in the Fig 6. It can be seen in the plot, that the softer `diskbb` component is dominant till $\sim$ 2.5keV while post that the harder `bbodyrad` component takes over.

The results for the best fit, using model (4.1), have been shown in Table 8 and Table 9 for Obs 1 and Obs 2 respectively. The polarimetric values obtained are consistent with the PCUBE analysis.

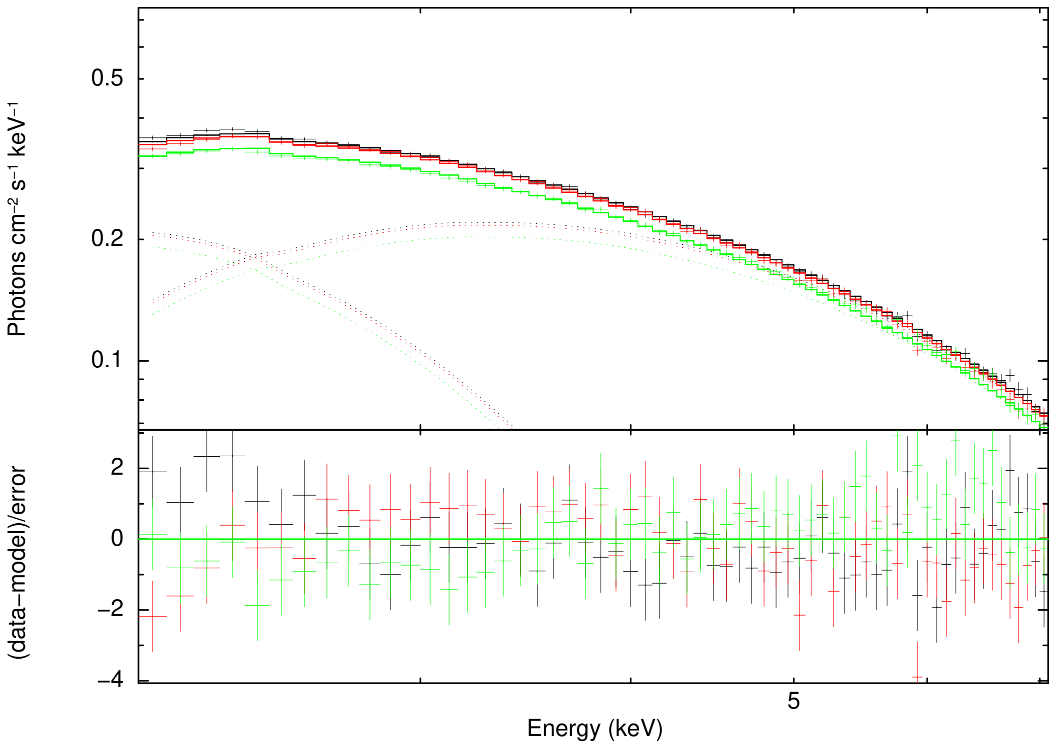

Figure 6: The unfolded intensity spectra for XTE J1701-462 (Obs 1), fitted with the model <`const`> * <`tbabs`> * (<`diskbb`> + <`bbodyrad`>).

XTE J1701-462	(Obs 1)	**Present Work**	**Published results**
polconst	*PD (%)*	5.69±0.33	4.58±0.37
	PA (deg)	-37.6±1.6	-37.7±2.3
tbabs	$N_H(10^{22}/cm^2)$	3.03±0.37	2.7±0.3
diskbb	T_{in} *(keV)*	$0.68^{+0.08}_{-0.05}$	$0.72^{+0.09}_{-0.07}$
	$R_{in}\sqrt{cos\ i}$ *(km)*	40^{+30}_{-26}	37^{+16}_{-12}
bbodyrad	*T (keV)*	$1.37^{+0.03}_{-0.02}$	$1.31^{+0.03}_{-0.02}$
	R_{bb} *(km)*	16±5	18±3
const	*DU 1*	1	1
	DU 2	0.983±0.003	0.981±0.003
	DU 3	0.92±0.003	0.917±0.003
χ^2/d.o.f		583/558	459/440

Table 8: Values obtained for XTE J1701-462 (Obs 1), in 2-8 keV range, compared to the published work by Cocchi et al. 2023, for the model-dependent analysis. Errors are in the 1-σ range.

For Obs 1, a systematic error of 1% was added. The value obtained for PD is $5.69 \pm 0.33\%$ compared to $4.58 \pm 0.37\%$ which was obtained by the published work by Cocchi et al. 2023, and are in agreement in 2-σ range. They have used the same baseline model for the analysis. The PA obtained is $-37.6 \pm 1.6°$ compared to the published value of $-37.7 \pm 2.3°$ by the same authors, and they agree completely. Similarly, the rest of the parameters too are within 1-σ range. Constrains on the inner radius ($R_{in}\sqrt{cos\ i}$), the source radius (R_{bb}) appear to be large. The varying normalised calibration constant (*const*) values for the three detectors depict the differences in the three corresponding spectra of the detectors. The contour plot for the PD and PA values for Obs 1 has been shown in Fig 7.

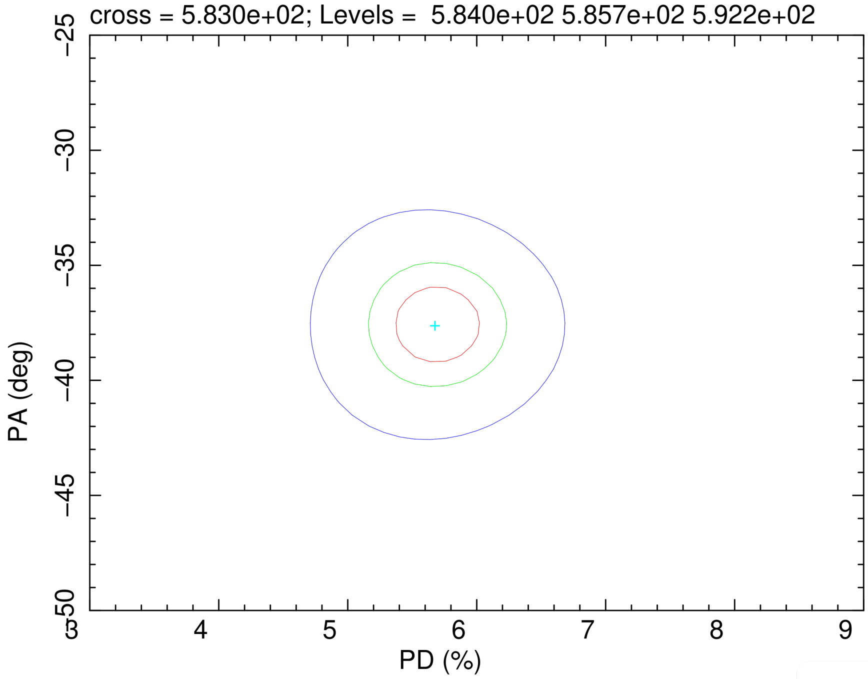

Figure 7: Polarization contours obtained for Obs 1 of XTE J1701-462, for the confidence levels of 1-σ, 90% and 3-σ respectively.

XTE J1701-462	(Obs 2)	**Present Work**	**Published results**
polconst	*PD (%)*	0.7±0.31	0.65±0.35
	PA (deg)	-55±13	-57±16
tbabs	$N_H (10^{22}/cm^2)$	$3.82^{+0.63}_{-0.39}$	$3.4^{+0.5}_{-0.3}$
diskbb	T_{in} *(keV)*	$0.50^{+0.04}_{-0.05}$	0.57±0.04
	$R_{in}\sqrt{cos\ i}$ *(km)*	69^{+65}_{-42}	78^{+35}_{-23}
bbodyrad	*T (keV)*	$1.19^{+0.01}_{-0.02}$	1.13±0.01
	R_{bb} *(km)*	21^{+7}_{-5}	26^{+4}_{-3}
const	*DU 1*	1	1
	DU 2	0.968±0.003	0.957±0.003
	DU 3	0.946±0.003	0.950±0.004
χ^2/d.o.f		560/558	456/440

Table 9: Values obtained for XTE J1701-462 (Obs 2), in 2-8 keV range, compared to the published work by Cocchi et al. 2023 for the model-dependent analysis. Errors are in the 1-σ range.

For the Obs 2, a systemtic error of 1.5% was applied and the value obtained for PD is $0.7 \pm 0.31\%$ compared to $0.65 \pm 0.35\%$ by the published work, and are within 1-σ confidence. The agreement is true in the case of the PA as well, with the values of $-55 \pm 13°$ and $-57 \pm 16°$ respectively. The remaining parameters are in close agreement too.

Comparing Obs 1 to Obs 2, it can be seen that PD obtained in Obs 1 is greater. Similarly, the BL temperature, and the inner disk temperature is greater in the case of Obs 1. But the radius of the inner disk increases from Obs 1 to Obs 2.

XTE J1701-462	(Obs 1)	**Present Work**	**Published results**
tbabs	$N_H(10^{22}/cm^2)$	3.03±0.37	2.7±0.3
diskbb	$T_{in}(keV)$	$0.68^{+0.08}_{-0.05}$	$0.72^{+0.09}_{-0.07}$
	$R_{in}\sqrt{cos\ i}\ (km)$	40^{+24}_{-23}	37^{+16}_{-12}
	$PD\ (\%)$	< 1.9	< 1.6
	$PA\ (deg)$	$PA_{BL} + 90$	$PA_{BL} + 90$
bbodyrad	$T\ (keV)$	$1.37^{+0.03}_{-0.02}$	$1.31^{+0.03}_{-0.02}$
	$R_{bb}\ (km)$	16±5	18±3
	$PD\ (\%)$	$7.43^{+0.47}_{-0.42}$	$6.14^{+0.69}_{-0.49}$
	$PA\ (deg)$	-38.1±1.6	-38.3±2.3
const	*DU 1*	1	1
	DU 2	0.983±0.003	0.981±0.003
	DU 3	0.92±0.003	0.917±0.003
χ^2/d.o.f		576/558	459/440

Table 10: Values obtained for Obs 1 of XTE J1701-462, compared to the published work by Cocchi et al. 2023, for the model-dependent analysis. Errors are in the 1-σ range.

Till now a combined polarization effect from both the components, the BL and the disk, was assumed. But the individual contribution of the components can further help in determining the characteristics of the geometry. Hence, a spectro-polarimetric analysis was performed for Obs 1, assuming that the components exhibit different polarization properties. Model 4.2 was used for this. The results have been shown in the Table 10. A parameter assumption was considered: the PA for disk was set at 90°, following the methodology of Farinelli et al. 2023. A reason for this is that, the intrinsic polarization arising from the two components, is orthogonal. The PD for the BL component was well constrained with the value of $7.43^{+0.47}_{-0.42}\%$, but only an upper limit of 1.9% was found in the case of disk polarization component. The PA of $-38.1 \pm 1.6°$ for the BL is consistent with PA found for overall polarization in Obs 1.

In the case of XTE J1701-462, Obs 1 was made when the source was in the HB of it's Z-track, and the Obs 2 was made during the NB evolution Cocchi et al. 2023. A considerable difference between the PD obtained for the two observations indicates a strong dependence of polarization on the source's evolution stage. The overall PD of ~5.7% in Obs 1 and the ~7.4% contribution from the BL component, is quite significant in the case of a LMXB. It's implications will be discussed in the further sections.

4.2.3 GX 9+9

With an orbital period of P $\sim$ 0.18 days, and at a distance of about 5 kpc (Kong et al. 2006), GX 9+9 is yet another LMXB hosting a neutron star. The mass of the compact object is around 1.4 $M_{\odot}$ while that of the optical companion is around 0.5 $M_{\odot}$ (Cornelisse et al. 2007). This binary system is classified as an atoll source, due to the 'C'-like shape it traces on a CCD. The average X-ray flux in the 2-20 keV band is $\sim$ 200 mCrab (Iaria et al. 2020). The system was discovered via a sounding rocket experiment way back in 1967 (Chatterjee et al. 2023). The intensity spectra has been depicted in the Fig 8, and has been fit with model 4.1.

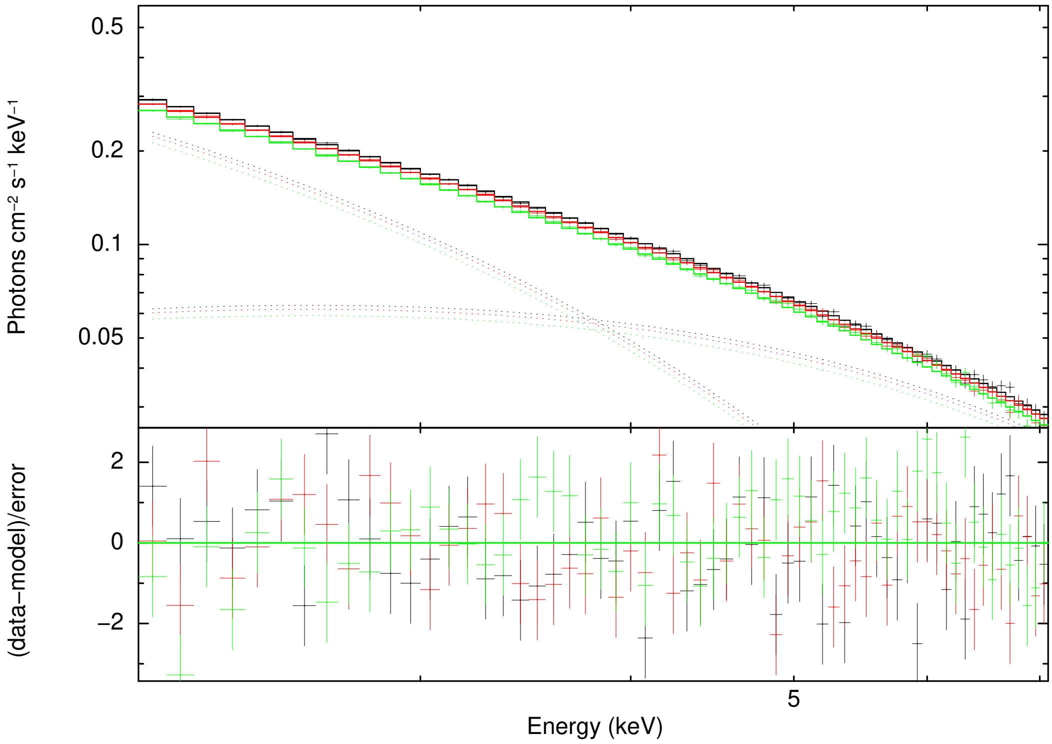

Figure 8: The unfolded intensity spectra for GX 9+9, fitted with the model 4.1.

The outcomes of the PCUBE analysis for GX 9+9 are presented in Table 11, alongside a comparative evaluation with the findings reported by Chatterjee et al. 2023. The PD within the 2-8 keV range was determined to be $1.02 \pm 0.34\%$, while within the narrower energy bands of 2-4 keV and 4-8 keV, it was found to be $0.79 \pm 0.4\%$ and $2.67 \pm 0.63\%$, respectively. It is noteworthy that the PD in the 2-4 keV band fell below the threshold of Minimum Detectable Polarization (MDP99), rendering it relatively insignificant.

Furthermore, the PA measurements spanning the energy ranges of 2-8 keV, 2-4 keV, and 4-8 keV were determined as $69.5 \pm 9.7°$, $72.5 \pm 14.5°$, and $63.4 \pm 6.8°$, correspondingly. Importantly, all retrieved PD and PA values are well-aligned with those documented by Chatterjee et al. 2023, falling within the 1-σ confidence interval.

The results obtained from the spectro-polarimetric analysis within the 2-8 keV range are summarized in Table 12. The PA for the disk component was set orthogonal to the BL component, following the procedure in Farinelli et al. 2023 and also followed in Ursini et al. 2023. The measured PD is $1.3 \pm 0.3\%$, with PA of $-68.1 \pm 7.4°$. These values lie comfortably within the 1-σ range of the PD and PA reported by

Ursini et al. 2023, which are $1.4 \pm 0.3\%$ and $-68 \pm 6°$, respectively. The contour plot for this analysis has been depicted in the Fig 9.

It is important to acknowledge the disparity in the underlying model, utilized between our analysis and that of Ursini et al. 2023. They employed a baseline model comprising the `diskbb` + `comptb` + `relxill` components, which integrates NuSTAR and IXPE data to derive parameter values. Particularly, the `relxillns` model, assumes a reflection of photons from the BL of the system off the accretion disk. The model `relxillns` is built upon the `relxillns`, and considers the illuminating spectrum incident at 45° to the disk surface (Ursini et al. 2023). This component helps in further differentiating the respective contributions of the individual components and holds significance for the discussion section.

	GX 9+9	**Present Work**	**Published Results**
2-8 keV	PD (%)	1.02 ±0.34	1.36±0.39
	PA (deg)	69.5±9.7	62.6±6.7
2-4 keV	PD (%)	0.79±0.4	0.94±0.38
	PA (deg)	72.5±14.5	71.4±11.5
4-8 keV	PD (%)	2.67±0.63	3.19±0.72
	PA (deg)	63.4±6.7	57.6±6.4

Table 11: Values for polarization degree (PD) and polarization angle (PA) obtained for GX 9+9 compared to the published work by Chatterjee et al. 2023, for PCUBE analysis. Errors are in the 1-σ range.

GX 9+9		**Present Work**	**Published results**
polconst	*PD (%)*	1.3±0.3	1.4±0.3
	PA (deg)	-68±7	-68±6
tbabs	$N_H(10^{22}/cm^2)$	$0.27^{+0.13}_{-0.07}$	
diskbb	$T_{in}(keV)$	$0.87^{+0.07}_{-0.06}$	
	$R_{in}\sqrt{cos\ i}$ *(km)*	16^{+3}_{-4}	
bbodyrad	*T (keV)*	$1.48^{+0.05}_{-0.04}$	
	R_{bb} *(km)*	7^{+3}_{-4}	
const	*DU 1*	1	
	DU 2	0.971±0.003	
	DU 3	0.926±0.003	
χ^2/d.o.f		566/558	

Table 12: Values obtained for GX 9+9, in 2-8 keV range, compared to the published work by Ursini et al. 2023, for model-dependent analysis. Errors are in the 1-σ range.

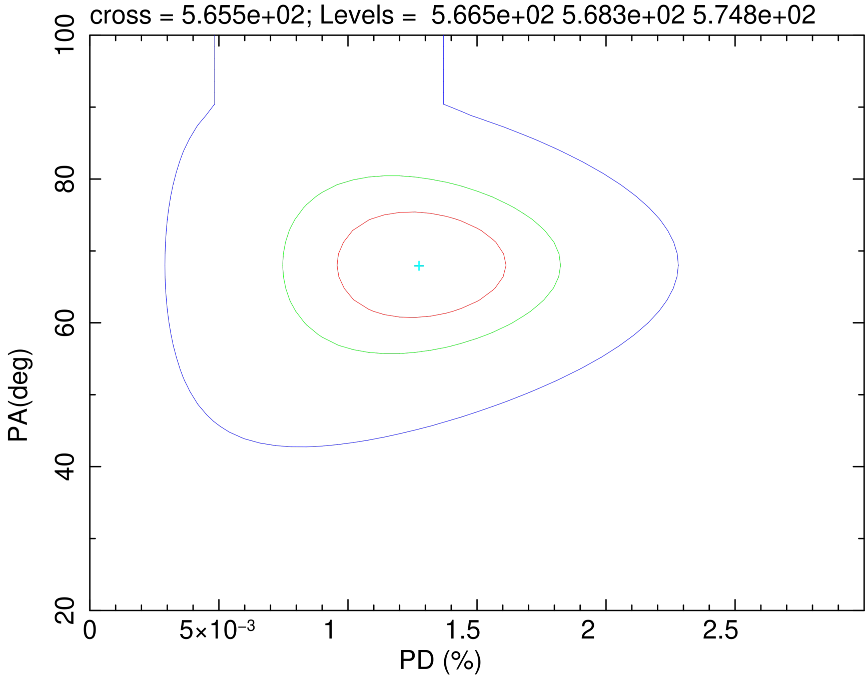

Figure 9: Polarization contour plot obtained for GX 9+9, in the 2-8 keV range, with contour levels of 1σ, 90% and 3σ.

Table 13 summarizes the results for individual component contribution for the spectro-polarimetric analysis using model 4.2. The disk component gives the PD of $1.68 \pm 1.16\%$, while the BL component exhibits a PD of $3.63^{+0.95}_{-0.92}\%$ and a PA of $67 \pm 6.1°$. The PA value for the disk component was again set at 90° to the BL component. The fit was obtained with a reduced χ^2 value of 1.002. The implications of these outcomes will be assessed in the discussion section.

GX 9+9		**Present Work**
tbabs	$N_H(10^{22}/cm^2)$	0.27±0.12
diskbb	T_{in} *(keV)*	$0.86^{+0.07}_{-0.06}$
	$R_{in}\sqrt{cos\ i}$ *(km)*	16^{+9}_{-8}
	PD (%)	1.68±1.16
	PA (deg)	$PA_{BL} - 90$
bbodyrad	*T (keV)*	$1.48^{+0.05}_{-0.04}$
	R_{bb} *(km)*	8^{+2}_{-3}
	PD (%)	$3.63^{+0.95}_{-0.92}$
	PA (deg)	67±6.1
const	*DU 1*	1
	DU 2	0.983±0.003
	DU 3	0.926±0.003
χ^2/d.o.f		558/557

Table 13: Values obtained for GX 9+9 compared to the published work by Ursini et al. 2023, for model-dependent analysis. Errors are in the 1-σ range.

4.2.4 GX 5-1

GX 5-1 is another LMXB which has been classified as a Z source. It lies at a distance of around 4.7 kpc (Clark 2018), however its orbital period is still open to investigation. While the compact object is a neutron star with a mass of $\sim 1.4\ M_{\odot}$, the mass of its counterpart is still unknown. The system is located at the Galactic centre (Kuulkers et al. 1994). Its location was found with a significant accuracy as a result of radio observations, which has also led to the belief of its companion likely being an infrared candidate (Jonker et al. 2000).

The results for the model independent PCUBE analysis for Obs 1 and Obs 2 have been shown in Table 14 and Table 15 respectively. In Obs 1, for the energy ranges of 2-8 keV, 2-4 keV and 4-8 keV, the PD found was $3.94 \pm 0.26\%$, $3.79 \pm 0.33\%$ and $4.67 \pm 0.42\%$ respectively. The PA values found were $-6.0 \pm 1.9°$, $-3.9 \pm 2.5°$ and $-12.8 \pm 2.6°$ in the corresponding intervals. Compared to the published value of PD of $4.3 \pm 0.3\%$ in 2-8 keV range by Fabiani et al. 2023, the analysed results falls in 1-σ confidence level and hence is in agreement. In Obs 2, the PD found was $1.83 \pm 0.25\%$, $1.82 \pm 0.31\%$ and $2.45 \pm 0.42\%$ in the ranges of 2-8 keV, 2-4 keV and 4-8 keV. For the same intervals, the corresponding PA found was $-11.5 \pm 4°$, $3.6 \pm 4.9°$ and $-19 \pm 5°$. The published result for the PD and PA values are within the 1-σ confidence range.

It can be observed the the PD is higher in the 4-8 keV range than 2-4 keV and it is consistent across both the observations. It suggests an energy dependence of the PD on the energy bands. In the work by Fabiani et al. 2023, they also have presented PCUBE analysis for 2-3 keV, 3-4 keV, 4-5 keV and 5-8 keV intervals between 2-8 keV. Their results for this show a consistent behaviour in both the observations across the energy ranges. However, it does not show a particular pattern of increase or decrease of the PD along the increasing energy range. Although, the energy range of 5-8 keV holds the highest PD value in an observation.

	GX 5-1 (Obs 1)	**Present Work**	**Published Results**
2-8 keV	PD (%)	3.94 ±0.26	4.3±0.3
	PA (deg)	-6.0±1.9	-9.7±2.0
2-4 keV	PD (%)	3.79±0.33	
	PA (deg)	-3.9±2.5	
4-8 keV	PD (%)	4.67±0.42	
	PA (deg)	-12.8±2.6	

Table 14: Values for polarization degree (PD) and polarization angle (PA) obtained for GX 5-1 (Obs 1) compared to the published work by Fabiani et al. 2023, for PCUBE analysis. Errors are in the 1-σ range.

	GX 5-1 (Obs 2)	**Present Work**	**Published Results**
2-8 keV	PD (%)	1.83 ±0.25	2.0±0.3
	PA (deg)	-11.5±4.0	-9.2±4.0
2-4 keV	PD (%)	1.82±0.31	
	PA (deg)	3.6±4.9	
4-8 keV	PD (%)	2.45±0.42	
	PA (deg)	-19±5	

Table 15: Values for polarization degree (PD) and polarization angle (PA) obtained for GX 5-1 (Obs 2) compared to the published work by Fabiani et al. 2023, for PCUBE analysis. Errors are in the 1-σ range.

GX 5-1 (Obs1)		Present Work	Published results
polconst	*PD (%)*	3.9±0.7	3.7±0.4
	PA (deg)	-10±5	-9±3
tbabs	$N_H(10^{22}/cm^2)$	$5.77^{+1.64}_{-1.62}$	
diskbb	$T_{in}(keV)$	$0.64^{+0.39}_{-0.12}$	
	$R_{in}\sqrt{cos\ i}$ *(km)*	52^{+27}_{-28}	
bbodyrad	*T (keV)*	$1.28^{+0.13}_{-0.06}$	
	R_{bb} *(km)*	18^{+10}_{-13}	
const	*DU 1*	1	
	DU 2	0.967±0.003	
	DU 3	0.95±0.003	
χ^2/d.o.f		568/558	

Table 16: Values obtained for GX 5-1 (Obs 1), in 2-8 keV range, compared to the published work by Fabiani et al. 2023, for model-dependent analysis. Errors are in the 1-σ range.

The results for the spectro-polarimetric analysis for Obs 1 have been summarized in the Table 16 using model 4.1 and in Table 17 using model 4.2. Systematic of 1.5% was added while performing the analysis. The PD obtained for model 4.1 was found to be $3.9 \pm 0.7\%$ and the PA to be $-10 \pm 5°$. The values are in 1-σ agreement with the published work of Fabiani et al. 2023, who have analysed the values to be $3.7 \pm 0.4\%$ and $-9 \pm 3°$ respectively. However, they have used a different baseline model. Their work also included the use of NuSTAR, NICER and IBIS/ISGRI data to first fir the X-ray spectra and then use those parameters to find the polarimetric values later by using IXPE.

The PD obtained for Obs 1 using model 4.2, for the disk component is $3.3 \pm 1.2\%$ and the PA is $25\pm11°$. The PD and PA for BL component is $5.1\pm0.5\%$ and $-16\pm3°$

respectively. The reduced χ^2 is 1.002. The temperature of the inner disk is around 0.64 keV in the case of Obs 1. The intensity spectra has been shown in the Fig 10, and the contour plot has been depicted in Fig 11.

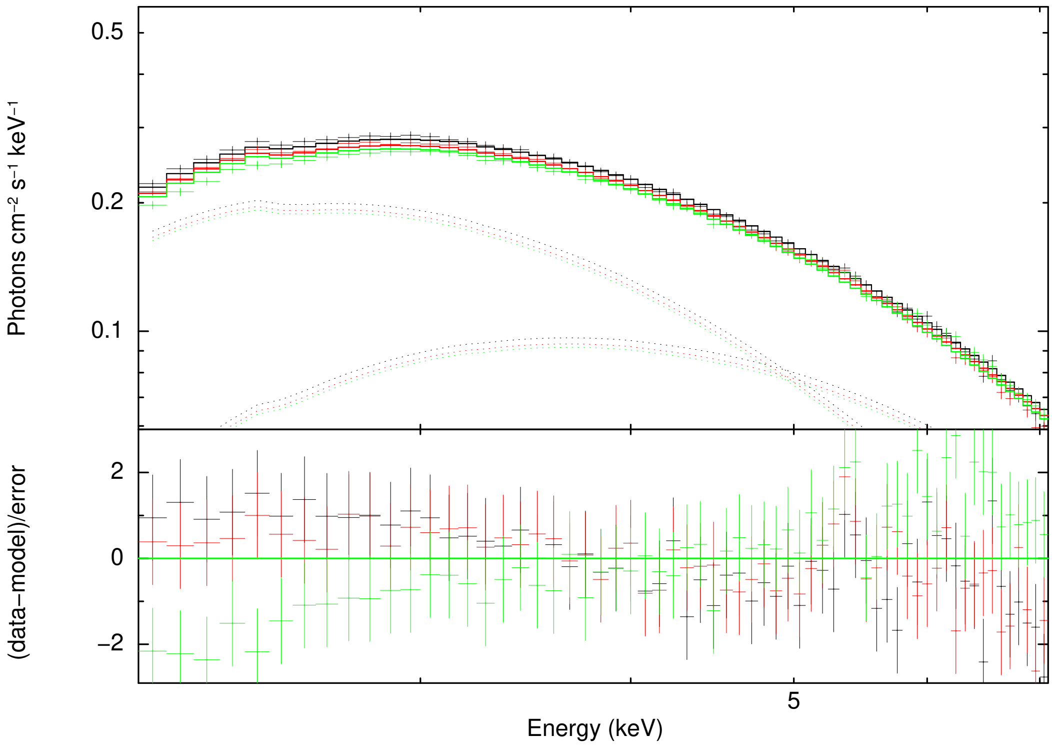

Figure 10: The unfolded intensity spectra for GX 5-1 (Obs 1), fitted with the model 4.1.

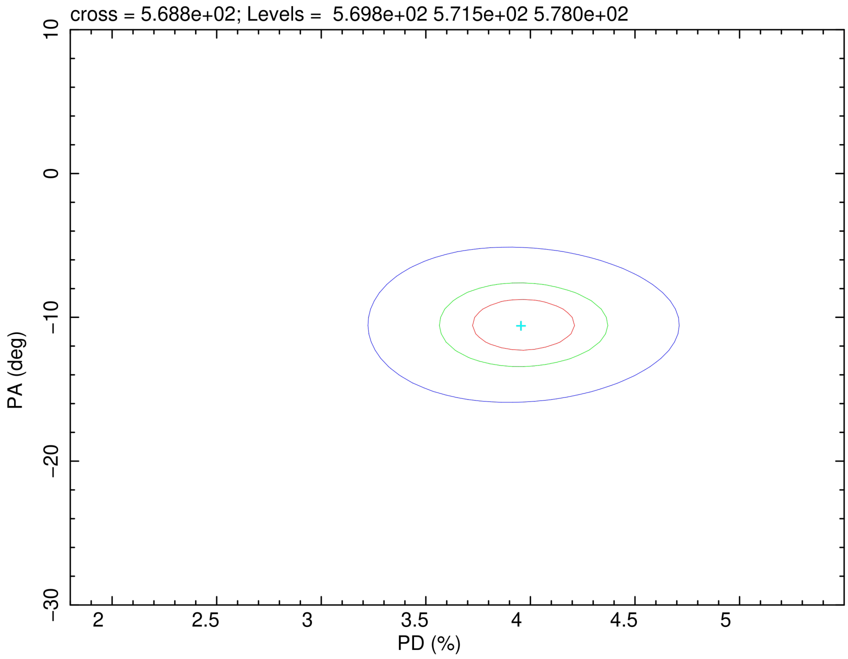

Figure 11: Polarization contours for PD and PA of GX 5-1 (Obs 1) in 2-8 keV range has been shown with confidence levels of 1σ, 90% and 3-σ.

GX 5-1 (Obs 1)		**Present Work**
tbabs	$N_H(10^{22}/cm^2)$	5.81±0.44
diskbb	T_{in} *(keV)*	$0.64^{+0.05}_{-0.04}$
	$R_{in}\sqrt{cos\ i}$ *(km)*	52^{+41}_{-34}
	PD (%)	3.3±1.2
	PA (deg)	25±11
bbodyrad	*T (keV)*	1.28±0.02
	R_{bb} *(km)*	18^{+5}_{-6}
	PD (%)	5.1±0.5
	PA (deg)	-16±3
const	*DU 1*	1
	DU 2	0.967±0.003
	DU 3	0.946±0.003
χ^2/d.o.f		558/557

Table 17: Values obtained for GX 5-1 (Obs 1) compared to the published work by Fabiani et al. 2023, for model-dependent analysis. Errors are in the 1-σ range.

For Obs 2, the spectro-polarimetric results using model 4.1 and 4.2 are shown in Table 18 and Table 19 respectively. Using the model 4.1, the values obtained for PD and PA are $1.9 \pm 0.2\%$ and $-8 \pm 4°$. Systematic of 1% was added. Compared to the published values by Fabiani et al. 2023, of $1.8 \pm 0.4\%$ for PD and $-9 \pm 6°$ for PA, the results are in agreement with each other. The inner disk temperature in Obs 2 is around 0.62 keV.

GX 5-1 (Obs 2)		**Present Work**	**Published results**
polconst	*PD (%)*	1.9±0.2	1.8±0.4
	PA (deg)	-8±4	-9±6
tbabs	$N_H (10^{22}/cm^2)$	5.97±0.36	
diskbb	$T_{in}(keV)$	$0.62^{+0.05}_{-0.04}$	
	$R_{in}\sqrt{cos\ i}$ *(km)*	60^{+44}_{-37}	
bbodyrad	*T (keV)*	$1.14^{+0.02}_{-0.01}$	
	R_{bb} *(km)*	23^{+6}_{-7}	
const	*DU 1*	1	
	DU 2	0.977±0.003	
	DU 3	0.935±0.003	
χ^2/d.o.f		566/558	

Table 18: Values obtained for GX 5-1 (Obs 2) compared to the published work by Fabiani et al. 2023, for model-dependent analysis. Errors are in the 1-σ range.

Using the model 4.2, the values of PD and PA obtained for the disk component are $3.2 \pm 1.2\%$ and $26 \pm 11°$, and for the BL component are $2.4 \pm 0.5\%$ and -20.7 ± 5.9 respectively. Unlike in the case of other sources, this time the PA for disk was not constrained and was set free to vary, following the methodology of Fabiani et al. 2023.

Comparing Obs 1 to Obs 2, a clear drop in the PD value can be seen in Obs 2. Since GX 5-1 is a Z-source, Fabiani et al. 2023 also plot the CCD and have shown that during the Obs 1 GX 5-1 was in its HB while during Obs 2, it was in the NB-FB. This correlation of PD with the evolution stage in the Z track was also noticed in the case of XTE J1701-462. However, there is no significant change in the corresponding inner disk temperature and same is the case for BL temperature too. In contrast, Fabiani et al. 2023 found the inner disk and BL temperature to be greater in Obs 2 than Obs 1. The BL sphere-equivalent radius and inner disk radius in the Obs 2 seem to larger, which again is in contrast with the published work.

GX 5-1 (Obs 2)		**Present Work**
tbabs	$N_H (10^{22}/cm^2)$	5.98±0.38
diskbb	T_{in} *(keV)*	$0.62^{+0.05}_{-0.04}$
	$R_{in}\sqrt{cos\ i}$ *(km)*	61^{+42}_{-38}
	PD (%)	3.2±1.2
	PA (deg)	26±11
bbodyrad	*T (keV)*	$1.14^{+0.02}_{-0.01}$
	R_{bb} *(km)*	23^{+7}_{-8}
	PD (%)	2.4±0.5
	PA (deg)	-21±6
const	*DU 1*	1
	DU 2	0.977±0.003
	DU 3	0.935±0.003
χ^2/d.o.f		559/556

Table 19: Values obtained for GX 5-1 (Obs 2) compared to the published work by Fabiani et al. 2023, for model-dependent analysis. Errors are in the 1-σ range.

5 Polarization of the boundary layer of neutron stars in X-ray binaries

In the previous chapter, results from the spectro-polarimetric analysis were presented for specific LMXBs. A detailed spectro-polarimetric analysis, assuming different sources of polarization corresponding to the disk and BL components of a NS, revealed some intriguing findings that demand further inspection. However, it was also observed that relying solely on IXPE data made it challenging to separate the polarization properties of the single components due to the limited energy band and energy resolution of the instrument. In studies by Farinelli et al. 2023 and Ursini et al. 2023, even after incorporating joint observations from IXPE and other X-ray observatories and using a Comptonized component for the BL, it remained difficult to discern the contribution of corresponding components.

The high degree of polarization for the BL, $\sim$7%, that was observed for XTE J1701-462 earlier, and also shown by the work of Cocchi et al. 2023, is difficult to explain as only a contribution of disk and comptanized emissions. Lapidus and Sunyaev 1985 considered polarization properties of X-ray busters modelled with an accretion disk and a BL. Excluding a direct emission from the disk, they have shown that the total PD of radiation emitted directly by the BL along with the fraction reflected off the disk, can give values of 6% for a viewing angle of around 70°. In their work for Cygnus X-2, Farinelli et al. 2023 suggest the presence of a reflection component, with polarization characteristics similar to that of the BL component. While Ursini et al. 2023, in their paper for GX 9+9, have shown the involvement of a reflection component (detected by NuSTAR) by incorporating it into their model, and that too led to a degeneracy. Results for the spectro-polarimetric analysis in this work are based upon a two-component model: disk and the BL. Further decomposition of individual contribution was not possible due to IXPE constraints and hence the high polarization shown by the BL component could as well be a cumulative of the original BL component and a different source of polarization - like a reflection off the disk. Hence, it becomes increasingly important to have a procedure for finding individual component contributions through theory and numerical simulations.

Motivated by these limitations, I participated in developing a simulation for calculating the polarization produced by the BL of a NS in LMXB conditions. This was carried out under the guidance of and in collaboration with Dr. Farinelli. Part of the study is inspired by the methodology followed by (Pihajoki et al. 2018, Bogdanov et al. 2019), which included light-bending effects of emission to the observer frame. However, their work was limited to X-ray Pulsars (XRPs) and only considered hotspots at the magnetic poles as a source of emission. In this work, an entire belt was considered around the NS up to a certain latitude, forming a BL.

To achieve the goal of determining the polarization properties of a BL, a two-step process was adopted: 1. First computing the PA and PD of radiation in the local rest frame (LRF). This was done by solving the radiative transfer equation (RTE) for polarized radiation in a plane-parallel geometry (slab). 2. Performing an angular integration for the radiation obtained in LRF, over the BL surface and calculating the total signal received in the observer frame. This was a function of inclination w.r.t the NS spin axis.

Going through the subsections, the solution to the RTE will be described in detail, and then the methodology for polarimetry of the BL will be looked at. Finally, the results will be presented followed by a short discussion. Contents of this chapter are based upon the research paper, that was published as a direct outcome of this work, by Farinelli et al. 2024. My contribution to the work involved merging the two steps effectively by first interpolating the results of step 1 that would be then fed to step 2 as an input, and make necessary customization throughout the analysis code for a precise execution of the simulation. The theoretical work presented in the upcoming section was done by Dr. Farinelli and has been shared here with his kind permission.

5.1 Solution of the radiative transfer equation

If it is assumed that I_l and I_r are the intensities with the electric field contained in the meridional plane and the one perpendicular to it, the total specific intensity can be described as $I = I_l + I_r$. In this context, the meridional plane is the one formed by the normal to the slab and the direction in which the electro-magnetic (EM) wave is propagating. In the case of a pure-scattering atmosphere, the equations will read like the following, in Thomson limits:

$$\mu \frac{dI_l}{d\tau} = -I_l + \frac{S_l}{2} + \frac{3}{8}\int_{-1}^{1} P_{1,1}(\mu,\mu')I_l(\mu')d\mu' + \frac{3}{8}\int_{-1}^{1} P_{1,2}(\mu,\mu')I_r(\mu')d\mu' \quad (5.1)$$

$$\mu \frac{dI_r}{d\tau} = -I_r + \frac{S_r}{2} + \frac{3}{8}\int_{-1}^{1} P_{2,1}(\mu,\mu')I_l(\mu')d\mu' + \frac{3}{8}\int_{-1}^{1} P_{2,2}(\mu,\mu^{'})I_r(\mu^{'})d\mu^{'} \quad (5.2)$$

here, μ is the cosine of the angle of the radiation beam with respect to the normal and $S_{l,r}(\tau)$ is the source term. This term describes the distribution of the seed photons over τ. These coupled RTEs have the unknowns of $I_{l(\mu,\tau)}$, $I_{r(\mu,\tau)}$ and with iterative procedures, these could be solved with appropriate boundary conditions, similar to Sunyaev and Titarchuk 1985 (hereafter ST85). Here $S_l = S_r = \frac{1}{2}S$. The Chandrashekhar scattering matrix $P_{i,j}(\mu,\mu')$ can be written as:

$$P_{1,1}(\mu,\mu') = 2(1-\mu^2)(1-\mu'^2) \quad (5.3)$$

$$P_{1,2}(\mu,\mu') = \mu^2 \quad (5.4)$$

$$P_{2,1}(\mu,\mu') = \mu'^2 \quad (5.5)$$

$$P_{2,2}(\mu,\mu') = 1 \quad (5.6)$$

Now, a distribution of photons over τ can be considered, which escape without scattering. If the scattering terms are excluded, we are left with the source function ($S(\tau)$) and the absorption term ($I_{l,r}$). The absorption in this case is related to the loss of photon intensity in the direction μ as the Thomson scattering leads to diffuses outside of the part of incoming photons in direction μ. Thus, the equations simplify to:

$$\mu \frac{dI_l}{d\tau} = -I_l + \frac{S}{2} \tag{5.7}$$

$$\mu \frac{dI_r}{d\tau} = -I_r + \frac{S}{2} \tag{5.8}$$

This set of equations has the following general solution:

$$I_{l,r}(\mu, \tau) = C_1 e^{-\tau/\mu} + \frac{1}{2\mu} \int_0^{\tau} e^{-(\tau-\tau')/\mu} S(\tau') d\tau' \tag{5.9}$$

The base of the slab is set at $\tau = 0$ and the top at $\tau = 2\tau_0$. $C_1 = 0$ is obtained as a consequence of the condition that incident radiation at the base of the slab $I(\mu, 0)$ $= 0$. For the seed photons that are located at the base of the atmosphere $S(\tau) =$ $S_0\delta(\tau)$, we get the following solution:

$$I_{l,r} = \frac{S_0}{2\mu} e^{-\tau/\mu} \qquad \mu > 0 \tag{5.10}$$

$$I_{l,r} = 0 \qquad \mu < 0 \tag{5.11}$$

If the seed photons are distributed uniformly as $S(\tau) = S_0$:

$$I_{l,r} = \frac{S_0}{2}(1 - e^{-\tau/\mu}) \qquad \mu > 0 \tag{5.12}$$

$$I_{l,r} = \frac{S_0}{2}\left[1 - e^{-(2\tau_0-\tau)/\mu}\right] \qquad \mu < 0 \tag{5.13}$$

These two sets of of equations will be henceforth labeled as; Case 1: where the seed photons are the base (eqn 5.10) and Case 2: in which seed photons are uniformly distributed (eqn 5.12).

Next, it can be considered that the radiation is subject to k-scattering $I^k_{l,r}$. In this case, the source term disappears, and this time the integral terms remain in the equation. These terms represent the contribution to the specific intensity along the direction μ, from all other directions. This contribution is a result of both photons that remain in the same polarization mode (e.g., $I_l^{k-1} \to I_l^k$), and also those that

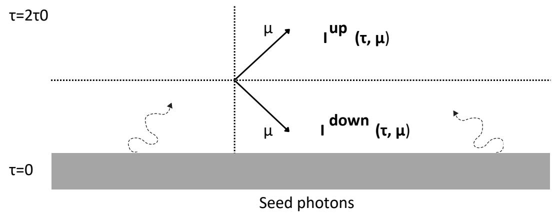

Figure 1: The sketch depicts the plane-parallel geometry of a slab for the radiative transfer problem, with seed photons at the base (Case 1).

switch from one mode to the other. Now the equations look like:

$$\mu\frac{dI_l^k}{d\tau} = -I_l^k + \frac{3}{8}\int_{-1}^{1} P_{1,1}(\mu,\mu')I_l^{k-1}(\mu')d\mu' + \frac{3}{8}\int_{-1}^{1} P_{1,2}(\mu,\mu')I_r^{k-1}(\mu')d\mu' \quad (5.14)$$

$$\mu\frac{dI_r^k}{d\tau} = -I_r^k + \frac{3}{8}\int_{-1}^{1} P_{2,1}(\mu,\mu')I_l^{k-1}(\mu')d\mu' + \frac{3}{8}\int_{-1}^{1} P_{2,2}(\mu,\mu')I_r^{k-1}(\mu')d\mu' \quad (5.15)$$

The integration is over the range $\mu' \in$ [-1 : 1]. Then the intensity can be classified as *upstream* intensity $I_u(\mu,\tau)$ which is directed towards the upper layer of the slab; and *downstream* intensity $I_d(\mu,\tau)$ which is directed towards the bottom layer of the slab (Fig 1). In this configuration, with τ computed from the bottom layer and progressively increasing, $I_u(\mu,\tau)$ corresponds to $\mu > 0$ and $I_d(\mu,\tau)$ to $\mu < 0$.

With a change of coordinates where $\tau \rightarrow 2\tau_0 \rightarrow -\tau$, a reference frame pointing downwards from the top of the slab, $I_d(\mu < 0,\tau)$ can be interchanged with $I_d(\mu > 0,\tau)$. Then, each scattering term within the integrals can be split into two components, with the angular integration in the range $\mu' \in [0 : 1]$.
When k = 1 is set, it can be seen from eqn 5.10 that

$$I_u^0(\mu,\tau) = \frac{S}{2\mu}e^{-\tau/\mu} \quad (5.16)$$

$$I_d^0(\mu, 2\tau_0 - \tau) = 0 \quad (5.17)$$

In more general form (let us consider for example the l-mode)

$$\int_{-1}^{1} P_{i,j}(\mu,\mu')I_l^{k-1}(\tau,\mu')d\mu' = \int_{0}^{1} P_{i,j}(\mu,\mu')\left[I_{\mathrm{u},l}^{k-1}(\tau,\mu') + I_{\mathrm{d},l}^{k-1}(2\tau_0-\tau,\mu')\right]d\mu' \quad (5.18)$$

The fact that the intensities $I_{r,l}(\mu,\tau)$ are now expressed as the contribution of the upstream and downstream factors, implies that from the practical point of view the algorithm numerically solves *four* differential equations over the domain $\mu \in [0:1]$

$$\mu\frac{dI^k_{u,l}}{d\tau} = -I^k_{u,l} + \frac{3}{8}\int_0^1 P_{1,1}(\mu,\mu')\left[I^{k-1}_{u,l}(\mu',\tau) + I^{k-1}_{d,l}(\mu',2\tau_0-\tau)\right]d\mu' \tag{5.19}$$

$$+\frac{3}{8}\int_0^1 P_{1,2}(\mu,\mu')\left[I^{k-1}_{u,r}(\mu',\tau) + I^{k-1}_{d,r}(\mu',2\tau_0-\tau)\right]d\mu' \tag{5.20}$$

$$\mu\frac{dI^k_{u,r}}{d\tau} = -I^k_{u,r} + \frac{3}{8}\int_0^1 P_{2,1}(\mu,\mu')\left[I^{k-1}_{u,l}(\mu',\tau) + I^{k-1}_{d,l}(\mu',2\tau_0-\tau)\right]d\mu'$$

$$+\frac{3}{8}\int_0^1 P_{2,2}(\mu,\mu')\left[I^{k-1}_{u,r}(\mu',\tau) + I^{k-1}_{d,r}(\mu',2\tau_0-\tau)\right]d\mu' \tag{5.21}$$

$$\mu\frac{dI^k_{d,l}}{d\tau} = -I^k_{d,l} + \frac{3}{8}\int_0^1 P_{1,1}(\mu,\mu')\left[I^{k-1}_{u,l}(\mu',2\tau_0-\tau) + I^{k-1}_{d,l}(\mu',\tau)\right]d\mu' \tag{5.22}$$

$$+\frac{3}{8}\int_0^1 P_{1,2}(\mu,\mu')\left[I^{k-1}_{u,r}(\mu',2\tau_0-\tau) + I^{k-1}_{d,r}(\mu',\tau)\right]d\mu' \tag{5.23}$$

$$\mu\frac{dI^k_{d,r}}{d\tau} = -I^k_{d,r} + \frac{3}{8}\int_0^1 P_{2,1}(\mu,\mu')\left[I^{k-1}_{u,l}(\mu',2\tau_0-\tau) + I^{k-1}_{d,l}(\mu',\tau)\right]d\mu'$$

$$+\frac{3}{8}\int_0^1 P_{2,2}(\mu,\mu')\left[I^{k-1}_{u,r}(\mu',2\tau_0-\tau) + I^{k-1}_{d,r}(\mu',\tau)\right]d\mu' \tag{5.24}$$

The upstream components $I^k_{u,l}$ and $I^k_{u,r}$, when computed from bottom to top, are solved by the first two equations of the above system. The other two are solved for the downstream components of $I^k_{d,l}$ and $I^k_{d,r}$ with τ from top to bottom. Once defined the seed photons distribution $S(\tau)$, the algorithm first seeks for a solution $I^0_{l,r}(\mu,\tau)$ as defined in Equation (5.10) or (5.12) and then starts to iterate the four-equations system (5.19).

From the theoretical point of view, the general solution of RTE (5.1) is obtained for *a given direction* μ. However, as we are interested in studying the angular dependence with respect to the normal of the polarization and specific intensity emerging from a slab as a function of both the total optical depth $2\tau_0$ as well as the seed photons distribution $S(\tau)$, we must define a grid of values μ_i. Instead of N-values μ_i equally stepped over the interval between 0 and 1, it is more convenient to use the roots of the Gauss-Legendre (GL) quadrature rule. The GL quadrature is used for numerical computation of the integral of functions bounded over the interval $x \in [a:b]$ according to

$$\int_a^b f(x)dx \approx \sum_{i=0}^{N-1} f(x_i)w(x_i) \tag{5.25}$$

where $a < x_i < b$ are the roots and $w(x_i)$ are the weights. The numerical algorithm then, actually solves iteratively the system (5.19) for each root μ_i, which is the best choice as these roots are used for the numerical integrals over $d\mu'$ according to equation (5.25).

By definition, the iterative method provides the solution for each scattering order $I^k(\mu, \tau)$. We are interested in the the following quantities at the top of the slab ($\tau = 2\tau_0$), where it is assumed that an observer is located:

1) Angular distribution of the total radiation $I^{\rm tot}(\mu) = I_l^{\rm tot}(\mu) + I_r^{\rm tot}(\mu)$ (limb-darkening law)

2) Angular distribution of the total polarization $P^{\rm tot}(\mu)$

we may define the total polarization

$$P^{\rm tot}(\mu) = \frac{I_r^{\rm tot}(\mu) - I_l^{\rm tot}(\mu)}{I_r^{\rm tot}(\mu) + I_l^{\rm tot}(\mu)} \tag{5.26}$$

It can be noticed that, $P(\mu)$ can be positive or negative. With the Stokes parameters $U = 0$, here P=Q. Let us have a look at the polarization angle

$$\chi = \frac{1}{2}\mathrm{Arc}Tan\frac{U}{Q} \tag{5.27}$$

When $Q > 0$, we have $\chi = \frac{1}{2}ArcTan0^{+}$=0, otherwise $\chi = \frac{1}{2}\mathrm{Arc}Tan0^{-} = \frac{1}{2}\pi$.

Thus, positive values of $P(\mu)$ will correspond to polarization angle along the slab (i.e. perpendicular to the normal), for negative values, the polarization angle is instead aligned with the normal of the slab.

Another parameter which in the end deserves to be checked is the percentage of the flux emerging from the top of the slab. Using the definition of flux and the GL quadrature rule we have

$$F^{\rm up} = \sum_{i=0}^{N-1} I_u^{\rm tot}(\mu_i)\mu_i w(\mu_i) \tag{5.28}$$

$$F^{\mathrm{down}} = \sum_{i=0}^{N-1} I_d^{\mathrm{tot}}(\mu_i)\mu_i w(\mu_i) \tag{5.29}$$

$$\epsilon = \frac{F^{\mathrm{up}}}{F^{\mathrm{up}} + F^{\mathrm{down}}} \tag{5.30}$$

The quantity ϵ will depend on the total optical depth of the slab and the seed photon distribution $S(\tau)$.

5.2 Polarimetry of the boundary layer

According to our earlier configuration, the top of the slab corresponds to the surface of the BL in the comoving frame. Hence, the PD and PA found in 5.26 and 5.27 are in the comoving frame too. We need to move from the comoving frame to the observer frame. The formalism for passing this has been developed to study the spectropolarimetric properties of accreting XRPs by Poutanen 2020. In this work, we expanded upon the methodology by making a change in the contribution to the total PD and PA observed, from just two spots at the magnetic poles to an equatorial belt covering the NS surface up to a given latitude θ^{max}. The additive property of the Stokes parameters makes it possible to compute the quantities as the contribution from each elementary area $d\Sigma'$ at the BL surface and then integrated over the domain $\theta \in [\pi/2\text{-}\theta^{max} : \frac{\pi}{2}]$ and $\phi \in [0 : 2\pi]$ (shown in Fig 2). Here,

$$d\sigma' = \gamma(\theta) R \sin\theta \ \mathrm{d}\theta \ \mathrm{d}\phi, \tag{5.31}$$

where $\gamma(\theta)$ is the Lorentz factor of the matter velocity at given latitude with

$$\beta(\theta) = \frac{2\pi R_{bl}}{c} \frac{\nu^{bl}}{\sqrt{1-\eta}} \sin\theta. \tag{5.32}$$

here, $\eta = R(g)/R_{nl}$ where $R_{bl} > R_{ns}$. In this work, we set $\eta = 1/2.5$ and we a BL co-rotating with NS si set at $\nu^{bl} = 500$ Hz.

For each elementary area dΣ' at coordinates θ and ϕ on the BL surface, one defines the Stokes vector in the observer frame as

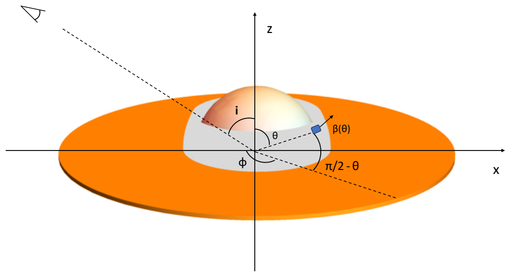

Figure 2: Proposed geometry for soft state of NS-LMXBs; the disk extends very close to the NS surface, and then a BL forms with $\Delta R \ll R_{ns}$. The BB photons from the NS photosphere are located at the base of the BL, which extends up to some latitude θ^{max} computed from the orbital plane, and has a given temperature kT_e and radial optical depth $2\tau_0$. Only photons in the northern hemisphere ($\theta < \pi/2$) reach the observer. The total signal is obtained by integrating the contribution from each elementary area $d\Sigma'$ shown by the blue box over the BL surface (Farinelli et al. 2024).

$$\mathcal{S} = I^{tot} d\Omega [1, P \cos 2\chi, P \sin 2\chi]. \tag{5.33}$$

where $d\Omega$ and $d\Sigma'$, along with I^{tot} and P are related via the Eqns. (17)-(20) of Poutanen 2020, and where χ is the PA w.r.t the projection of the NS spin onto the sky.

The Stokes vector was obtained by integrating $\mathcal{S}$ over $d\Omega$, to give $\mathcal{S}^{tot}$, and then the corresponding PD and PA were found out. The upper limit for the polar angle is $\theta = \pi/2$, due to total interception of the radiation from the southern hemisphere of BL and only receiving radiation from the northern hemisphere. The comoving frame of the specific intensity and PD is calculated by linear interpolation of the array of values that were stored in a text file and were preliminary computations for plane-parallel geometry. This was done for the 2-dimensional integration over the BL surface.

5.3 Results

In the numerical solution of the RTE 5.1 for polarized radiation we adopted a new different setup with respect to the case of ST85. The case of seed photons uniformly distributed across the slab is the same of ST85, but here we defined a new geometrical setup in which the seed photons are located at the base of the slab, unlike ST85 who considered a fully symmetric configuration along the vertical direction with seed photons at the center. We considered the cases of seed photons at the base and uniformly distributed across the slab. The plane-parallel geometry of an electron-scattering atmosphere located above a source of photons resembles a geometrically thin BL partially covering the NS surface, with $\Delta R \ll R_{ns}$, or even the atmosphere above the disk.

In Fig 3, the angular dependence of the total specific intensity and PD for seed photons located at the base (Case 1) and for different optical depths, are shown. The specific intensity values are normalized to the case for $\mu = 1$. For positive values of the PD, the PA is coplanar to the slab; for negative values, it is parallel to the normal. It can be seen that when $2\tau_0 \lesssim 1$, all the PD values are negative implying that PA is aligned along the slab normal. In the case of $2\tau_0 = 2$, the PA flip occurs at around $\mu \sim 0.3$ and when $2\tau_0 = 5$, the graph resembles the Chandrasekhar limit. In Case 2, where seed photons have uniform distribution, PD is negative for all the optical depths presented except for the initial small interval for $2\tau_0 = 5$. This can be seen in the Fig 4. In both cases though, the total intensity $I^{tot}(\mu)$ does not show a monotonic behaviour.

Once the values were adjusted by the shift of the comoving frame to the observer frame, the results can be seen in the figures 5, 6 and 7. A high optical depth is considered typical of the Comptonization component of NS-LMXBs in the soft state (Farinelli et al. 2023), and hence the higher values of $2\tau_0$ make an interesting case to look at. Here, two maximum latitudes of the BL were considered: $\theta^{max} = 45°$ and $\theta^{max} = 30°$ and in Fig 5, one can see the comparison of the two for $2\tau_0 = 5$. It can be seen that PD for $\theta^{max} = 45°$ is lower than that for $\theta^{max} = 30°$. This potentially is a direct result of the fact that a less extended BL is intrinsically "spherically less symmetric". The flux, when $\theta^{max} = 45°$, increases by ∼30% and for $\theta^{max} = 30°$ the observed flux is highest at $i \sim 50°$. In Fig 6 the PD, PA and normalized flux for $\theta^{max} = 45°$ for $\tau < 2\tau_0$ have been depicted for Case 1. In comparison with Fig 5, one can see a change of almost 90° in the PA. The higher the value of optical depth, the lesser the PD. From Fig 5 and 6 it can be seen that the PD is less than ∼1% in both instances, for higher values of $2\tau_0$ at $2\tau_0 = 5$ and $2\tau_0 = 2$.

In Fig 7, Case 2 (uniform seed photons) has been presented for $\theta^{max} = 45°$, over different values of the optical depth. The PD for $2\tau_0 = 5$ is comparable to the one

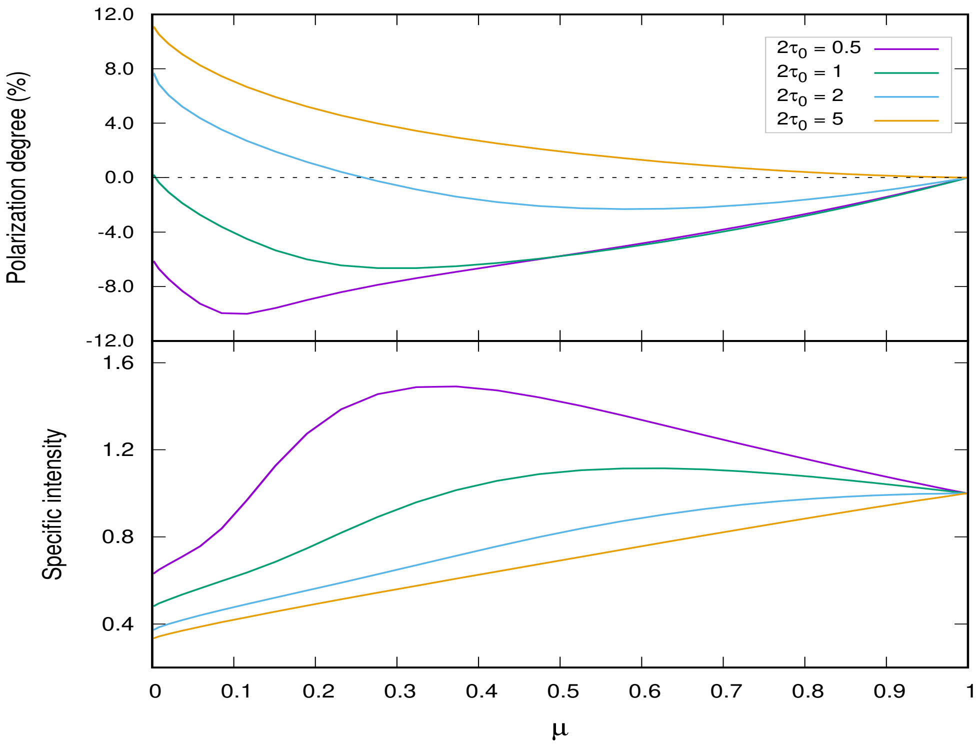

Figure 3: The graph depicts angular distribution of total PD (*upper panel*) and normalized specific intensity (*lower panel*) emerging from the upper layer of the slab for different values of the optical depth. The configuration of seed photons at the base of the slab has been considered (Case 1). For positive values of the PD, the PA is coplanar to the slab; for negative values it is parallel to the normal.

in Case 1, however the PA has flipped by 90°. The normalized flux decreases with an increase in the observer viewing angle. Since the polarization plane gets rotated because of the BL angular velocity, its effect can be seen on the PA, which is neither aligned perfectly to the NS spin nor perpendicular to it.

Since the numerical solutions provide for an individual contribution of the BL to the polarization, these results are a strong support to the spectro-polarimetric analysis of IXPE data. Some key inferences could be made from the results of the simulations, that were carried out for two different seed photon distributions over different values of optical depths. It was observed that only the optically thick configuration with seed photons at the base, gave PA which is almost aligned with the NS spin. The PD in such cases was seen to be $\lesssim$0.5%. The effect of light bending in the case of non-rotating NS/BL systems turned out to be $\lesssim$2%. When the spin frequency was set at $\nu^{bl} = 500$ Hz, the value for PA was slightly affected by $\sim$ 4°-7° for

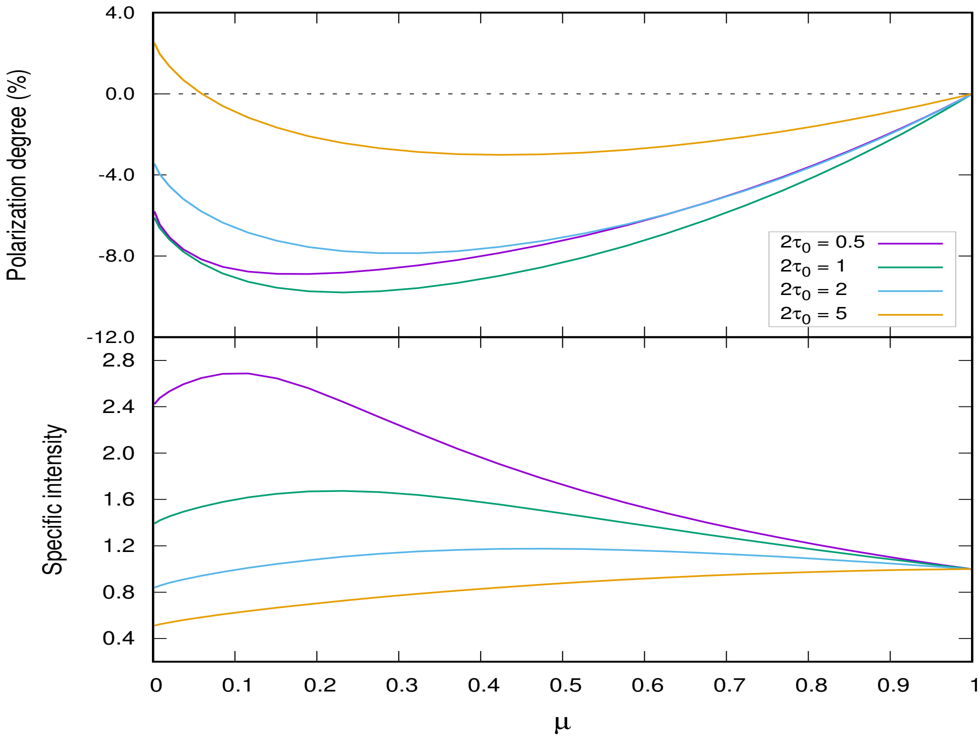

Figure 4: Same as Fig. 3, but for seed photons uniformly distributed over τ (Case 2).

both the θ^{max} (30° and 45°) considered. Finally, the upper limit on PD of the BL established here shows that at high optical depths, there is another component adding to the high percentage of PD attributed to the Comptonization component via the model-dependent spectro-polarimetric analysis. This exceeding part provides a strong contribution to the polarization values but does not affect the observed flux much. It is highly possible that this additional portion comes as a direct consequence of the reflection of radiation from the disc.

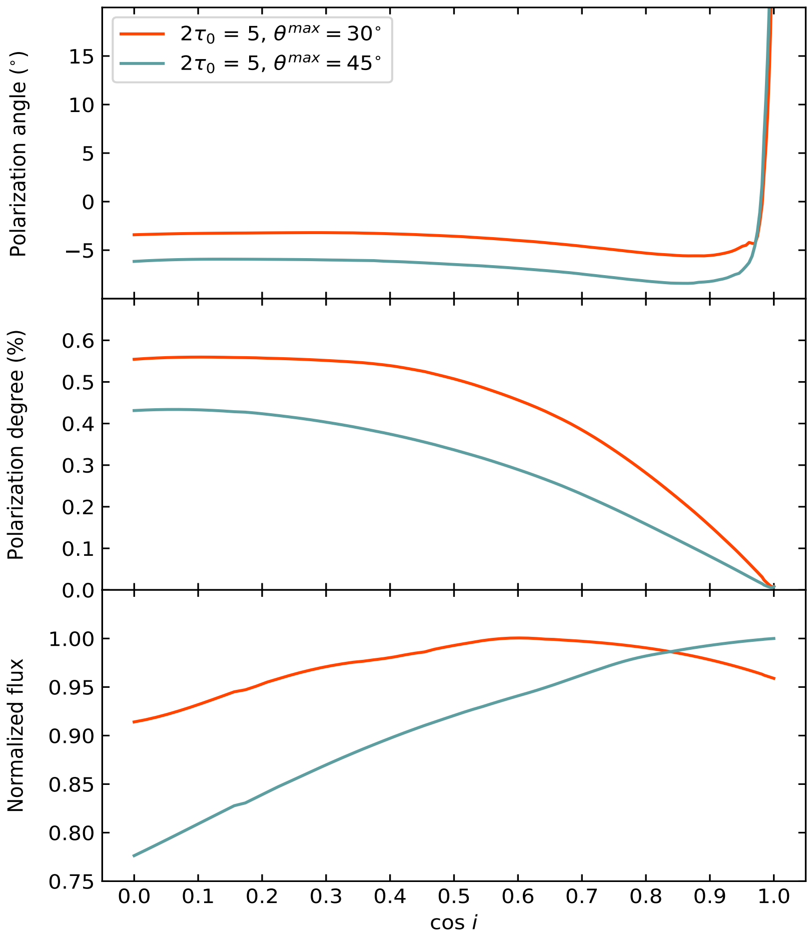

Figure 5: The graph depicts the total PA (*upper panel*), PD (*middle panel*), and normalized intensity (*lower panel*) of the BL as a function of the viewing angle with seed photons at the base of the slab (Case 1) for an optical depth of $2\tau_0$=5, spin frequency of ν_{bl} = 500 Hz, and two values of the BL latitude. The PA is measured with respect to the projection on the sky of the NS spin axis.

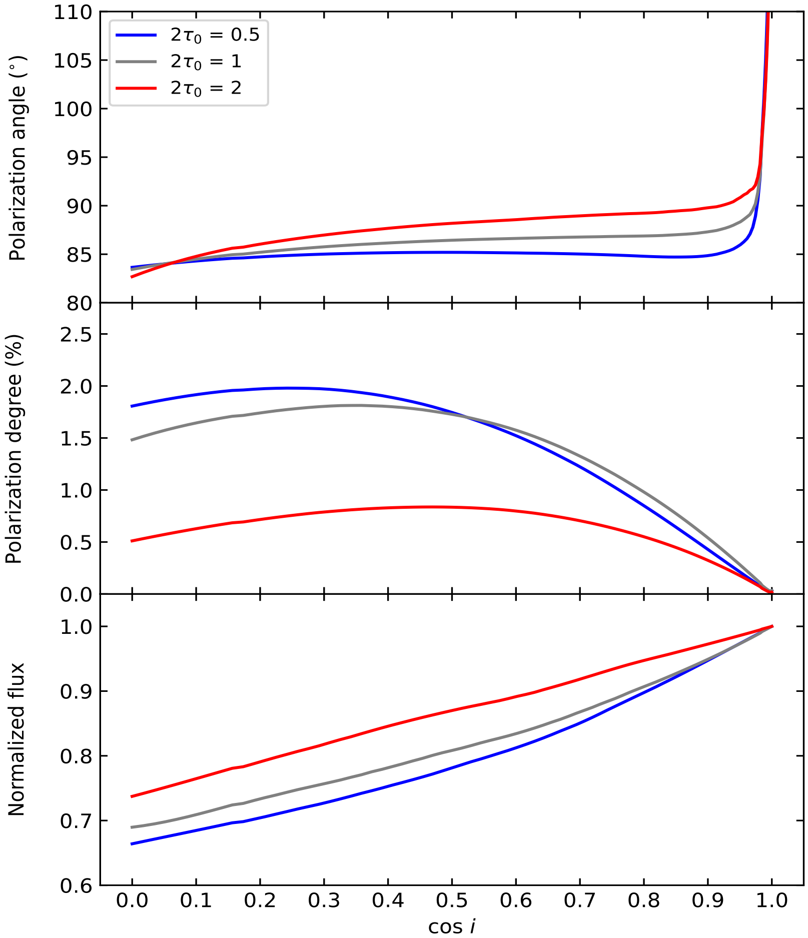

Figure 6: Same as in Fig. 5, but for different values of the optical depth and fixed BL latitude $\theta^{max} = 45°$ and spin $\nu_{bl} = 500$ Hz.

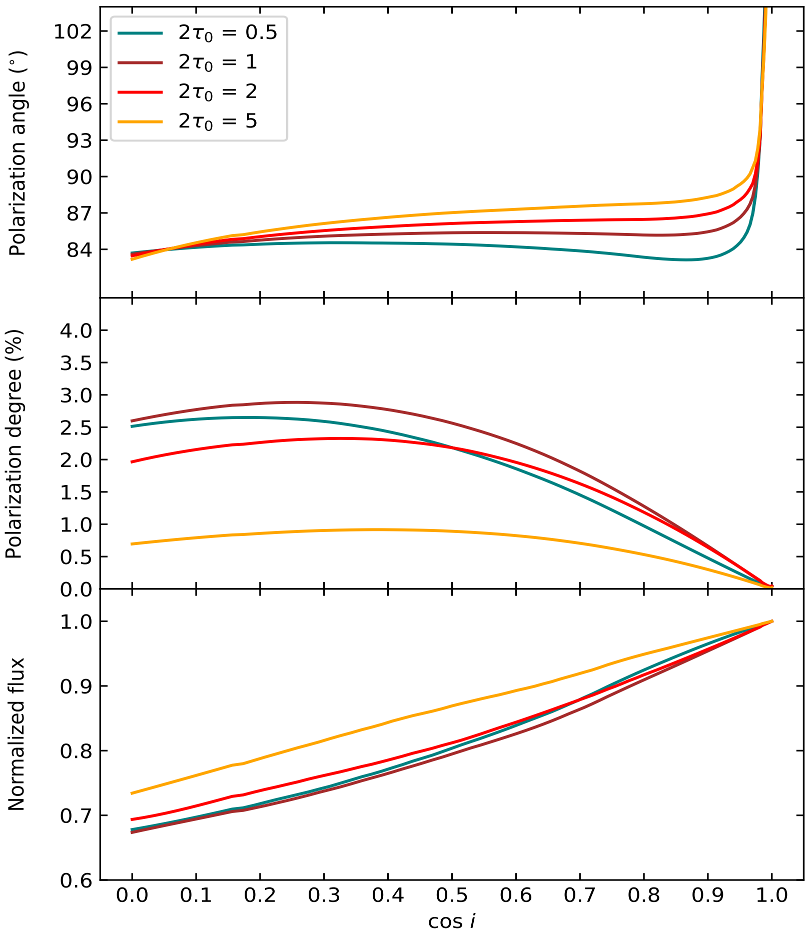

Figure 7: Same as Fig. 5, but with seed photons uniformly distributed (Case 2) and different values of the optical depth of the BL, with a latitude of $\theta^{max} = 45°$ and spin of $\nu_{bl} = 500$ Hz.

6 Discussion and Conclusions

In this thesis, an extensive spectro-polarimetric data analysis on four different NS-LMXBs, Cygnus X-2, XTE J1701-462, GX 9+9 and GX 5-1, using IXPE data, was presented. It was followed by a simulation analysis to determine the individual polarization of the BL of a NS-LMXB.

In the spectro-polarimetric analysis it was observed that the PD values in the case of XTE J1701-462 ($\sim$5.7%, Obs 1) and GX 5-1 ($\sim$3.9%, Obs 1) are much than the ones found in Cygnus X-2 ($\sim$1.2%, Obs 1) and GX 9+9 ($\sim$1.3%). Further investigation into individual contribution to polarization revealed that the PD contribution from the disk is around 2-3% in most of the observations. The classical results from Chandrasekhar 2003 predict the disk polarization to be around 2% when a high optical depth scattering atmosphere is assumed at an inclination of 60°.

For the BL component, the PD found was much more dominant than its disk counterpart. In the case of XTE J1701-462 ($\sim$7.4%, Obs 1) and GX 5-1 ($\sim$5%, Obs 1) it is tricky to justify such a significant value of PD. A PD of $\sim$10% could potentially be achieved via multiple Compton scatterings in a plane-parallel corona above the disk (Poutanen and Svensson 1996) assuming that it is optically thin, but such a spectral component was not seen in the IXPE data (Cocchi et al. 2023). There could also be another scenario where the emissions from the BL are carried in strong winds arising from the disk or a jet. However, there is no conclusive evidence of such an acceleration mechanism (Cocchi et al. 2023). Another possible mechanism that could be present is that of scattering of radiation in the wind above the disk (Sunyaev and Titarchuk 1985), where the emission after getting scattered can give rise to a high PD of around 27% at a 60° inclination.

Another prospect is the fact that maybe there are other contributions to the high PD observed from the BL component. A strong candidate is disk reflection. Lapidus and Sunyaev 1985 have shown that a PD of $\sim$4-5% can be achieved via such mechanism.

The problem is that the IXPE's limited energy band and energy resolution do not allow to clearly disentangle the contribution to the net observed polarization signal from the single regions of the system, leaving in turn to a degeneracy problem. Then, if we fit the IXPE spectrum with a (<diskbb> + <bbodyrad>) model, we are actually describing the system with a two-component model, while in fact at least a third contribution comes from disk reflection. As the latter is not included in the spectro-polarimetric analysis, its high contribution to the PD is falsely attributed to the blackbody feature. Ursini et al. 2023 in their spectral analysis of GX 9+9, using data from other observatories than IXPE, have hinted at a reflection component as a source of polarization. This argument is also supported by the increase of the inner disk radius from Obs 1 to Obs 2 which was seen in the cases of XTE J1701-462 and GX 5-1. As the inner disk radius increased, a clear drop in the PD was seen. This is obvious if reflection from the disk indeed does act as a prominent polarization source. Once the radius increases, the latitudinal extent of the BL decreases and thus the disk is not illuminated efficiently (Cocchi et al. 2023). Another relation that can be established is that Obs 2 in Z-sources was in the NB/FB while Obs 1 was during the HB. It could be said that a Z-source exhibits high polarization when the source is in its HB. IXPE's inability to discern between the individual component contributions makes it increasingly important to find other ways to constrain the contributions. Hence, a simulation for calculating the BL polarization was carried out.

The simulation work assumed a slab-like, plane-parallel, geometry that emulates a BL extended up to a certain latitude (30° and 45°). Considering a high optical depth, typical to a NS-LMXB, and seed photons located at the base of the slab, it was seen that the PD obtained for the BL is less than ∼0.5%. Any excessive PD obtained via model-dependent spectro-polarimetric analysis for the BL, hence indicates an external contribution to the rise of the PD observed. The PA in such cases was found to be parallel to the NS spin axis, although slightly rotated by a few degrees. The variation is possibly due to light bending in strong gravity. This result is in agreement with the analysed values for Cygnus X-2 and validates the polarimetric results of the simulation. Hence, an upper limit on the BL PD was obtained through this work, indirectly also constraining the effects of external contributions to the observed PD in the BL component. Fig 1, depicts the different possible polarization sources in a LMXB.

Through this work, it could be established that using IXPE data alone for spectro-polarimetric analysis proves to be difficult to constrain different components in the model, owing majorly to the limited spectral range of the instrument. Even then, valuable insights could be obtained from the analysis and put constraints on the polarization mechanisms and geometry of the LMXBs. The simulation work was further able to put limits on the BL polarization thus indicating the presence of a reflective component or some other mechanism, in addition to the disk polarization and the Comptonized BL polarization. The degeneracy of spectral fitting of IXPE data could be resolved to an extent via fusing data with other observatories, however, limitations still creep up for the spectro-polarimetric analysis. Future X-ray polarimetry missions such as the enhanced X-ray Timing and Polarimetry mission (eXTP), boasting a broader spectral range and an added feature of timing, present a promising opportunity to build upon the foundational framework established by IXPE.

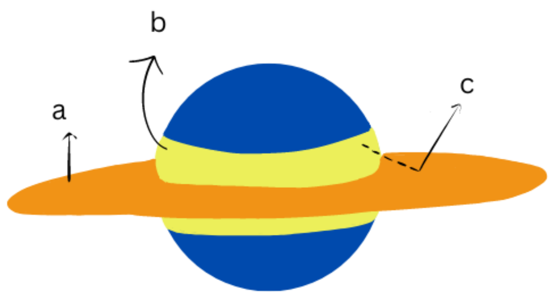

Figure 1: The sketch of a neutron star (in blue), surrounded by an accretion disk (in orange), and a BL (in yellow), depicts the different possible sources of polarized emission: (a) photons emerging from the disk could be inherently polarized. (b) photons emerging from the BL could be inherently polarized. (c) photons originating from the BL and then impinging on the disk to further getting reflected off from it, also present a scenario of strong polarization.

Acknowledgements

This thesis would not have been possible without the strong support of wonderful people around me.

Firstly, I would like to express my heartfelt gratitude to Prof. Santangelo for his constant support and guidance throughout my master's studies and thesis. His contagious energy and passion for Astrophysics have set high standards, which have constantly pushed me towards bettering myself at each stage.

I also want to sincerely thank Dr. Ducci, for his patience and constant support at every step of my thesis. His calm demeanour and humility allowed me the freedom to execute things at a comfortable pace which helped me to get the best out of the experience.

Dr. Farinelli's invaluable support has been crucial for me throughout the entire journey. His willingness to allow me to learn from my mistakes and his faith in my potential has been a huge boost.

I want to thank Dr. Doroshenko for helping me get started with the thesis and for his timely guidance.

Lastly, I would like to thank my family for their endless encouragement, as their sacrifices and unwavering belief have been the foundation for my success.

Bibliography

Bahramian, A. and N. Degenaar (2023). “Low-Mass X-ray Binaries”. In: *Handbook of X-ray and Gamma-ray Astrophysics*. Springer Nature Singapore, pp. 1–62.

Baldini, L., N. Bucciantini, N. D. Lalla, S. Ehlert, A. Manfreda, M. Negro, N. Omodei, M. Pesce-Rollins, C. Sgrò, and S. Silvestri (2022). “ixpeobssim: A simulation and analysis framework for the imaging X-ray polarimetry explorer”. In: *SoftwareX* 19, 101194, p. 101194.

Bałucińska-Church, M., Gibiec, A., Jackson, N. K., and Church, M. J. (2010). “On the nature of the Cygnus X-2 like Z-track sources”. In: *Astronomy and Astrophysics*.

Bambi, C. and A. Santangelo (2022). *Handbook of X-ray and Gamma-ray Astrophysics*. Springer Singapore.

Baptista, R. (2001). “Eclipse Mapping of Accretion Discs”. In: *Astrotomography, Indirect Imaging Methods in Observational Astronomy*. Ed. by H. M. J. Boffin, D. Steeghs, and J. Cuypers. Vol. 573.

Bogdanov, S., F. K. Lamb, S. Mahmoodifar, M. C. Miller, S. M. Morsink, T. E. Riley, T. E. Strohmayer, A. K. Tung, A. L. Watts, A. J. Dittmann, D. Chakrabarty, S. Guillot, Z. Arzoumanian, and K. C. Gendreau (2019). “Constraining the Neutron Star Mass-Radius Relation and Dense Matter Equation of State with NICER. II. Emission from Hot Spots on a Rapidly Rotating Neutron Star”. In: *The Astrophysical Journal Letters* 887.1, L26, p. L26.

Campana, S. and T. Di Salvo (2018). “Accreting Pulsars: Mixing-up Accretion Phases in Transitional Systems”. In: *Astrophysics and Space Science Library*. Vol. 457. Astrophysics and Space Science Library, p. 149.

Casares, J., P. Charles, and E. Kuulkers (1998). “The Mass of the Neutron Star in Cygnus X-2 (V1341 Cygni)”. In: 493.1, pp. L39–L42. arXiv: `astro-ph/9711236 [astro-ph]`.

Chakrabarty, D. and P. Roche (1997). “The Symbiotic Neutron Star Binary GX 1+4/V2116 Ophiuchi”. In: *The Astrophysical Journal* 489.1, pp. 254–271.

Chandrasekhar, S. (2003). “Radiative Transfer”. In: *Dover Publications*.

Chatterjee, R., V. K. Agrawal, K. M. Jayasurya, and T. Katoch (2023). “Spectro-polarimetric view of bright atoll source GX 9+9 using IXPE and AstroSat”. In: *Monthly Notices of the Royal Astronomical Society* 521.1, pp. L74–L78.

Chou, Y. (2014). “Measuring the orbital periods of low mass X-ray binaries in the X-ray band”. In: *Research in Astronomy and Astrophysics* 14.11, pp. 1367–1382.

Clark, G. W. (2018). “Monte Carlo Simulation of the X-Ray Halos of GX 5-1 and GX 13+1 to Test Models of Insterstellar Dust Grains”. In: 852.2, 121, p. 121.

Cocchi, M. et al. (2023). “Discovery of strongly variable X-ray polarization in the neutron star low-mass X-ray binary transient XTE J1701462”. In: *Astronomy and Astrophysics* 674, p. L10.

Cornelisse, R., D. Steeghs, J. Casares, P. A. Charles, A. D. Barnes, R. I. Hynes, and K. O’Brien (2007). “Optical spectroscopy of the low-mass X-ray binary GX9+9”. In: 380.3, pp. 1219–1229.

Cowley, A. P., D. Crampton, and J. B. Hutchings (1979). “The halo population X-ray source Cygnus X-2.” In: *Astrophysical Journal* 231, pp. 539–550.

Fabiani, S. et al. (2023). “Discovery of a variable energy-dependent X-ray polarization in the accreting neutron star GX 5-1”. In: *arXiv e-prints*, arXiv:2310.06788.

Farinelli, R. et al. (2023). “Accretion geometry of the neutron star low mass X-ray binary Cyg X-2 from X-ray polarization measurements”. In: *Monthly Notices of the Royal Astronomical Society* 519.3, pp. 3681–3690.

Farinelli, R., A. Waghmare, L. Ducci, and A. Santangelo (2024). “The polarization of the boundary layer around weakly magnetized neutron stars in X-ray binaries”. In: *arXiv e-prints*, arXiv:2401.16239, arXiv:2401.16239.

Hasinger, G. and M. van der Klis (1989). “Two patterns of correlated X-ray timing and spectral behaviour in low-mass X-ray binaries.” In: *Astronomy and Astrophysics* 225, pp. 79–96.

Iaria, R., S. M. Mazzola, T. Di Salvo, A. Marino, A. F. Gambino, A. Sanna, A. Riggio, and L. Burderi (2020). “Reflection component in the Bright Atoll Source GX 9+9”. In: *Astronomy and Astrophysics* 635, A209.

Jayasurya, K. M., V. K. Agrawal, and R. Chatterjee (2023). “Detection of significant X-ray polarization from transient NS-LMXB XTE J1701-462 with IXPE and its implication on the coronal geometry”. In: *Monthly Notices of the Royal Astronomical Society* 525.3, pp. 4657–4662.

Jin, Y. K., S. N. Zhang, and J. F. Wu (2006). “Hardness Ratio Estimation in Low Counting X-Ray Photometry”. In: *The Astrophysics Journal* 653.2, pp. 1566–1570.

Jonker, P. G., R. P. Fender, N. C. Hambly, and M. van der Klis (2000). “The infrared counterpart of the Z source GX 5-1”. In: 315.4, pp. L57–L60.

Kislat, F., B. Clark, M. Beilicke, and H. Krawczynski (2015). “Analyzing the data from X-ray polarimeters with Stokes parameters”. In: *Astroparticle Physics* 68, pp. 45–51.

Kong, A. K. H., P. A. Charles, L. Homer, E. Kuulkers, and D. O’Donoghue (2006). “Simultaneous X-ray/optical observations of GX9+9 (4U1728-16)”. In: 368.2, pp. 781–795.

Kuulkers, E., M. van der Klis, T. Oosterbroek, K. Asai, T. Dotani, J. van Paradijs, and W. H. G. Lewin (1994). “Spectral and correlated timing behaviour of GX5-1.” In: 289, pp. 795–821.

Lapidus, I. I. and R. A. Sunyaev (1985). “Angular distribution and polarization of X-ray-burster radiation (during stationary and flash phases)”. In: *Monthly Notices of the Royal Astronomical Society* 217.2, pp. 291–303.

Lin, D., D. Altamirano, J. Homan, R. A. Remillard, R. Wijnands, and T. Belloni (2009a). “Type I X-ray Bursts from the Neutron-star Transient XTE J1701-462”. In: *The Astrophysics Journal* 699.1, pp. 60–65.

Lin, D., R. A. Remillard, and J. Homan (2009b). “Spectral States of XTE J1701 - 462: Link Between Z and Atoll Sources”. In: *The Astrophysical Journal* 696.2, pp. 1257–1277.

Maccarone, T. J., J. van den Eijnden, T. D. Russell, and N. Degenaar (2020). “Eclipses of jets and discs of X-ray binaries as a powerful tool for understanding jet physics and binary parameters”. In: *Monthly Notices of the Royal Astronomical Society* 499.1, pp. 957–973.

Mignani, R., A. Shearer, A. Słowikowska, S. M. Zane, A. Shearer, and S. Z. Agnieszka Słowikowska (2019). *Astronomical Polarisation from the Infrared to Gamma Rays.*

Negro, M. et al. (2023). “The IXPE View of GRB 221009A”. In: *The Astrophysical Journal Letters* 946.1, L21, p. L21.

Orosz, J. A. and E. Kuulkers (1999). “The optical light curves of Cygnus X-2 (V1341 Cyg) and the mass of its neutron star”. In: *Monthly Notices of the Royal Astronomical Society* 305.1, pp. 132–142.

Pihajoki, P., M. Mannerkoski, J. Nättilä, and P. H. Johansson (2018). “General Purpose Ray Tracing and Polarized Radiative Transfer in General Relativity”. In: *The Astropysics Journal* 863.1, 8, p. 8.

Popham, R. and R. Sunyaev (2001). “Accretion Disk Boundary Layers around Neutron Stars: X-Ray Production in Low-Mass X-Ray Binaries”. In: *The Astrophysical Journal* 547.1, pp. 355–383.

Poutanen, J. (2020). “Relativistic rotating vector model for X-ray millisecond pulsars”. In: *Astronomy and Astrophysics* 641, A166, A166.

Poutanen, J. and R. Svensson (1996). “The Two-Phase Pair Corona Model for Active Galactic Nuclei and X-Ray Binaries: How to Obtain Exact Solutions”. In: *The Astrophysics Journal* 470, p. 249.

Reig, P. (2011). “Be/X-ray binaries”. In: *Astrophysics and Space Science* 332.1, pp. 1–29.

Remillard, R. A., D. Lin, ASM Team at MIT, and NASA/GSFC (2006). “New X-ray Transient, XTE J1701-462”. In: *The Astronomer’s Telegram* 696, p. 1.

Shapiro, S. L. and S. A. Teukolsky (1983). *Black holes, white dwarfs and neutron stars. The physics of compact objects.*

Spencer, R. E., A. P. Rushton, M. Bałucińska-Church, Z. Paragi, N. S. Schulz, J. Wilms, G. G. Pooley, and M. J. Church (2013). "Radio and X-ray observations of jet ejection in Cygnus X-2". In: *Monthly Notices of the Royal Astronomical Society* 435.1, pp. L48–L52.

Sunyaev, R. A. and L. G. Titarchuk (1985). "Comptonization of low-frequency radiation in accretion disks Angular distribution and polarization of hard radiation". In: *Astronomy and Astrophysics* 143.2, pp. 374–388.

Tauris, T. M. and E. P. J. Van Den Heuvel (2010). "Formation and evolution of compact stellar X-ray sources". In: *Compact Stellar X-ray Sources.*

Ursini, F. et al. (2023). "X-ray polarimetry and spectroscopy of the neutron star low-mass X-ray binary GX 9+9: An in-depth study with IXPE and NuSTAR". In: 676, A20, A20.

Wilms, J., A. Allen, and R. McCray (2000). "On the Absorption of X-Rays in the Interstellar Medium". In: *The Astrophysical Journal* 542.2, pp. 914–924.